NATIONAL TECHNICAL UNIVERSITY OF ATHENS
SCHOOL OF CIVIL ENGINEERING
DEPARTMENT OF STRUCTURAL ENGINEERING
STATICS AND ANTISEISMIC RESEARCH LABORATORY

Multiscale Finite Element Analysis

Postgraduate Dissertation

MARIA TAVLAKI

Supervisor: **VISSARION PAPADOPOULOS,** Assistant Professor, NTUA

ATHENS 2013

Contents

Table of Figures

Acknowledgements

I would like to express my sincere gratitude to Prof. Vissarion Papadopoulos for offering me the opportunity to complete this dissertation, for his guidance and his continuous support and motivation throughout the past months.

Introduction

The purpose of this thesis is the implementation and investigation of the first-order multi-scale homogenization process within a macroscopic framework. To this end, the homogenization solution scheme proposed by (Miehe & Koch, 2002) is used; in particular the algorithms pertaining to linear prescribed boundary displacements, as well as periodic boundary displacements and anti-periodic tractions. To illustrate the macroscopic effects of material non-linearity, a Representative Volume Element (RVE) consisting of a fiber embedded in a matrix is used, taking into account the slippage between the two. This model is combined with an existing bond-slip mathematical description. A cantilever beam consisting microscopically of the material described by the above RVE, submitted to a scaled vertical load is then analyzed using a nested solution scheme (FE^2) and the pushover curve of the structure is obtained. The above are organized in four chapters as follows:

In the first chapter, some basic concepts and assumptions of the first-order homogenization solution scheme are introduced, and the procedure is explained in detail. Moreover, the macroscopic nested solution scheme is outlined. In the second chapter, the bond-slip mathematical description is summarized. In Chapter 3 the model used for the analyses is presented, alongside the numerical results. Finally, the last chapter gives a brief summary of conclusions regarding the methods used.

1 First-Order Computational Homogenization

1.1 Introduction

Heterogeneous materials have been present in structures for a very long time. In fact, a very common structural material, concrete, is made up from entirely disparate materials. These heterogeneities have been treated in the past using empirical models. In the last few years however, the emergence of new, composite materials, which are created in a controlled manner from different base materials, in order to make use of the best qualities of each of their components, have created a demand for more accurate description of the phenomena occurring during their loading. The first approach towards that direction is the so-called “brute-force” approach; that is, the whole structure is meshed, including all the heterogeneities. This approach, although accurate, is very computationally intensive, thus practically impossible for bigger structures. In these cases, the use of the so-called “multi-scale” methods becomes more attractive.

These can be split into two big categories (Feyel, 2003):

1. *Sequential methods:* A detailed microscopic analysis yields the relevant mechanisms which are responsible for the macroscopic behavior. A macroscopic analysis is then performed, making use of these mechanisms. In essence, microscopic constitutive laws are formulated a priori, which are subsequently used for the description of the macroscopic behavior. The drawback of this method is that a lot of information about the interaction of the phases is lost in the process.
2. *Integrated Methods:* A discretization of the microstructure is used, and some homogenization rules are used to create a link between the macroscopic and microscopic behaviour. That is, we perform parallel computation on both the macroscopic and the microscopic level. The first-order homogenization, which is used in the current approach, fits in this category.

1.2 Basic Hypotheses

As described by (Kouznetsova, 2002), the material configuration is assumed to be sufficiently homogeneous at the macroscopic, but heterogeneous at the microscopic scale. The microscopic length is assumed much larger than the molecular dimensions, so that the continuum approach is justified, but sufficiently smaller than the characteristic size of the macroscopic sample or the wave length of the macroscopic loading, in the principle of the separation of scales.

As far as periodicity goes, it is a usual assumption that the structure displays global periodicity, that is, a single microscopic cell repeats itself in the whole macroscopic structure. However, the more realistic local periodicity assumption can be made, i.e. that there is a diversity of molecular structures at different macroscopic points, although the structures repeat themselves in a small vicinity of each individual macroscopic point. This is illustrated in Figure 1-2.

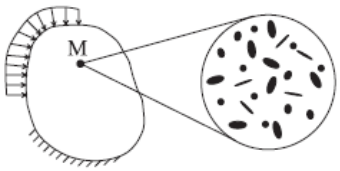

Figure 1-1
Representation of the micro- and macrostructure (Kouznetsova, 2002)

From this point onward, we assume that the microstructure at some macroscopic point is described by a Representative Volume Element (RVE). The size of the RVE should be small enough, so that it facilitates numerical computations, yet large enough, so that it represents the microstructure accurately, without introducing undesired anisotropy. We denote the macroscopic scale with the letter M, and the microscopic (RVE) with the letter m.

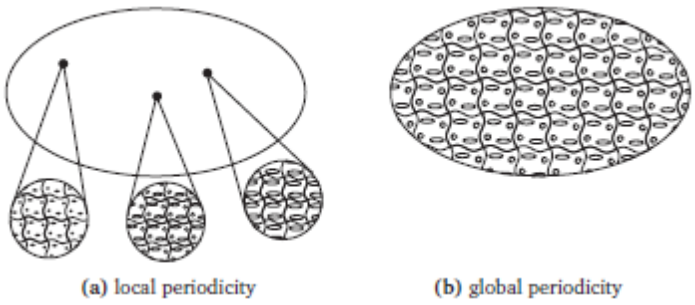

Figure 1-2
Schematic representation of global and local periodicity (Kouznetsova, 2002)

In the case of the first-order homogenization scheme, the nested solution scheme works as follows: Firstly, the macroscopic deformation gradient F_M (or the strain tensor ε, as we will see promptly) is calculated for every material point of the macroscopic structure. Then the deformation gradient is used to formulate the boundary conditions of the RVE. After the solution of the boundary value problem, the stress field (or the microscopic stress tensor P_m) and the tangential stiffness are known for every point of the RVE. This tensor is then used to calculate the macroscopic stress tensor P_M by averaging the microscopic stresses of the RVE, as well as the macroscopic tangent stiffness. (See Figure 1-3.)

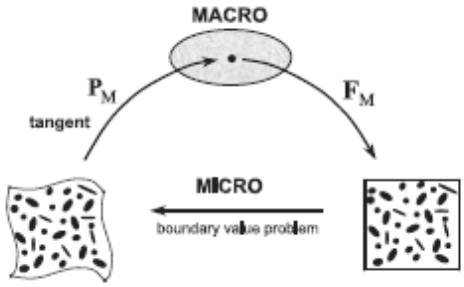

Figure 1-3
Schematic Representation of micro-macro transition (Kouznetsova, 2002)

1.3 Nested Solution Scheme (FE²)

After the relevant mechanical scales are chosen, FE² models are constructed using three main ingredients:

a. a modelling of the mechanical behaviour at the lower scale;
b. a localization rule which determines the local solutions inside the unit cell, for any given overall strain.
c. a homogenization rule giving the macroscopic stress tensor, knowing the micromechanical stress state-that is, establishing a connection between the macroscopic and microscopic stress.

The above approach, where the macroscopic strain dictates the microscopic deformation (in our case, the boundary displacements), is called “deformation driven”.

In the case of the Finite Element Analysis using a Newton-Raphson iterative procedure, the procedure followed can be summarized in the following steps:

MACROSCALE		**MICROSCALE**
1. Discretize the macroscopic model, assign a RVE at each Gauss Point Select the applied load and discretize it in increments		
	⟶	Discretize the microscopic model
2. Initialization • initialize the macroscopic model • assign zero strain to every macroscopic Gauss Point		
	⟶	• Prescribe the boundary conditions, according to the macroscopic strain • Solve the Boundary Value Problem, taking into consideration the current boundary conditions and the loading history • Calculate the tangential stiffness matrix $\boldsymbol{k}$ • Calculate the tangential Macroscopic Elasticity Matrix $\bar{\mathbb{C}}$ as a function of the tangential stiffness matrix $\boldsymbol{k}$
• Calculate the macroscopic tangent stiffness matrix $\boldsymbol{K} = \int \boldsymbol{B^T} \bar{\mathbb{C}} \boldsymbol{B} dA$	⟵	
3. Next increment • Apply next increment of the macroscopic load		
4. Next iteration • solve the macroscopic system • calculate the strain at every macroscopic Gauss Point		

⟶

- Prescribe the boundary conditions, according to the macroscopic strain
- Solve the Boundary Value Problem, taking into consideration the current boundary conditions and the loading history
- Calculate the nodal force vector $\boldsymbol{f}$
- Calculate the tangential stiffness matrix $\boldsymbol{k}$
- Calculate the homogenized macroscopic strain $\overline{\boldsymbol{\sigma}}$, as a function of the nodal force vector $\boldsymbol{f}$
- Calculate the tangential Macroscopic Elasticity Matrix $\overline{\mathbb{C}}$ as a function of the tangential stiffness matrix $\boldsymbol{k}$

⟵

- Calculate the macroscopic tangent stiffness matrix $\boldsymbol{K}$
- Calculate the macroscopic nodal force vector $\boldsymbol{F} = \int \boldsymbol{B^T}\overline{\boldsymbol{\sigma}}dA$
- Check for convergence
  i. If convergence is achieved, go to Step 2
  ii. Else, go to Step 3

The following chapters elaborate on the derivation of the homogenized macroscopic strain $\overline{\boldsymbol{\sigma}}$ and the Macroscopic Elasticity Matrix $\overline{\mathbb{C}}$.

1.4 Definition of a microequilibrium state (Miehe & Koch, 2002)

We consider a microstructure $\mathcal{B} \subset \mathcal{R}^3$ with overall properties related to a homogenized macrocontinuum $\overline{\mathcal{B}} \subset \mathcal{R}^3$, as visualized in Figure 1-4. Typically, the microstructure defines a representative volume (RV) of a nonlinear heterogeneous material such as inelastic composite, polycrystalline aggregate or particle assembly.

Let $\{\boldsymbol{u}: \mathcal{B} \times \mathcal{R} \to \mathcal{R}^3\}$ denote the displacement field at a material point $\boldsymbol{x} \in \mathcal{B}$ and a time $t \in \mathcal{R}$ of the microstructure $\mathcal{B} \subset \mathcal{R}^3$, and $\boldsymbol{\varepsilon} \coloneqq sym[\nabla \boldsymbol{u}]$ be the microscopic strain. Furthermore, we introduce the velocity field $\dot{\boldsymbol{u}} \coloneqq \partial_t \boldsymbol{u}(\boldsymbol{x}, t)$ and the acceleration field $\ddot{\boldsymbol{u}} \coloneqq \partial_{tt}^{\boldsymbol{2}} \boldsymbol{u}(\boldsymbol{x}, t)$ of the microstructure.

We assume a dynamic equilibrium state

$$\mathrm{div}\boldsymbol{\sigma} - \rho_0 \ddot{\boldsymbol{u}} = \boldsymbol{0} \quad \text{in } \mathcal{B} \tag{1.1}$$

where the symmetric stress $\boldsymbol{\sigma}$ is assumed to be related to the strain $\boldsymbol{\varepsilon}$ by some solid material model, for example, an elastic constitutive equation

$$\boldsymbol{\sigma} = \partial_{\varepsilon} \widehat{\boldsymbol{\psi}}\,(\boldsymbol{\varepsilon}, \boldsymbol{x}) \text{ in } \mathcal{B}, \tag{1.2}$$

governed by a strain energy function $\widehat{\boldsymbol{\psi}}$. Integrating the conditions 1.1 over the domain $\mathcal{B}$, and applying the Gauss theorem, yields the global conditions of equilibrium:

$$\int_{\partial \mathcal{B}} \boldsymbol{t} dA - \int_{\mathcal{B}} \rho_0 \ddot{\boldsymbol{u}}\, dV = \boldsymbol{0} \text{ and } \int_{\partial \mathcal{B}} \boldsymbol{x} \times \boldsymbol{t} dA - \int_{\mathcal{B}} \boldsymbol{x} \times \rho_0 \ddot{\boldsymbol{u}}\, dV = \boldsymbol{0} \tag{1.3}$$

where

$$\boldsymbol{t} \coloneqq \boldsymbol{\sigma}\boldsymbol{n} \text{ on } \partial \mathcal{B} \tag{1.4}$$

denotes the traction field on the surface with outward normal $\boldsymbol{n}$ at $\boldsymbol{x} \in \partial \mathcal{B}$. The equilibrium state of the microstructure $\mathcal{B}$ is assumed to be consistent with certain boundary conditions for the displacement $\boldsymbol{u}$, which relate the deformation of the microstructure to a prescribed macroscopic strain mode $\boldsymbol{\varepsilon}(t)$. These boundary conditions are formulated consistent with an averaging theorem in Chapter 1.5 below.

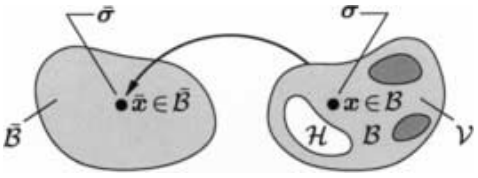

Figure 1-4
The notion of a continuum with microstructure. (Miehe & Koch, 2002)
Associated with a typical point $\bar{x} \in \bar{\mathcal{B}}$ of a homogenized macrocontinuum $\bar{\mathcal{B}} \subset \mathcal{R}^3$ is a microstructure $\mathcal{B} \subset \mathcal{R}^3$. The representative volume $\mathcal{V} \subset \mathcal{R}^3$ that characterizes a representative part of the heterogeneous material, contains a solid part $\mathcal{B}$ and a hole part $\mathcal{H}$, i.e. $\mathcal{V} = \mathcal{B} \cup \mathcal{H}$. $\bar{\sigma}$ and σ denote the macroscopic and microscopic Cauchy stress fields at $\bar{x} \in \bar{\mathcal{B}}$ and $x \in \mathcal{B}$, respectively.

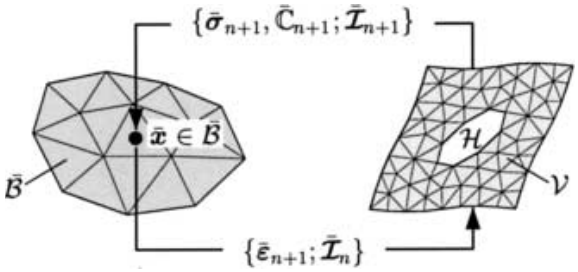

Figure 1-5

Strain-driven computational treatment of a discretized microstructure. (Miehe & Koch, 2002)
In a typical incremental step, the microstructure $\mathcal{V}$ is ''loaded'' by the advanced macroscopic strain $\bar{\varepsilon}_{n+1}$. The enforcement of an incremental (dynamic) equilibrium state associated with the microstructure yields at $\bar{x} \in \bar{\mathcal{B}}$ homogenized values of the macrostresses $\bar{\sigma}_{n+1}$, the macromoduli $\mathbb{C}_{n+1}$ and the internal state variables $\mathcal{I}_{n+1}$

1.5 Basic macrovariables and the averaging theorem (Miehe & Koch, 2002)

Let $\mathcal{V} \subset \mathcal{R}^3$ denote the RV associated with the microstructure $\mathcal{B} \subset \mathcal{R}^3$. This volume is assumed to consist of the solid part $\mathcal{B}$ and the hole part $\mathcal{H}$. Thus we consider the decompositions of the RV and the surface of the solid part

$$\mathcal{V} = \mathcal{B} \cup \mathcal{H} \text{ and } \partial\mathcal{V} = \partial\mathcal{B} \cup \partial\mathcal{H}\,, \tag{1.5}$$

see Figure 1-4.

1.5.1 Deformation

According to the first of the averaging relations, the macroscopic strain $\bar{\boldsymbol{\varepsilon}}$ should be equal to the volume average of the microscopic strain $\boldsymbol{\varepsilon}$.

$$\bar{\boldsymbol{\varepsilon}} = \frac{1}{|\mathcal{V}|}\int_{\mathcal{V}} \boldsymbol{\varepsilon}\, dV \tag{1.6}$$

Taking into account that $\boldsymbol{\varepsilon} \coloneqq sym[\nabla \boldsymbol{u}]$, and making use of the divergence theorem, we get:

$$\bar{\boldsymbol{\varepsilon}} = \frac{1}{|\mathcal{V}|}\int_{\mathcal{V}} sym[\nabla \mathbf{u}]\, dV \Leftrightarrow$$
$$\boxed{\bar{\boldsymbol{\varepsilon}} = \frac{1}{|\mathcal{V}|}\int_{\partial\mathcal{V}} sym[\mathbf{u} \otimes \mathbf{n}]\, dA} \tag{1.7}$$

1.5.2 Stress

Similarly, the averaging relation for the stress is established as:

$$\bar{\boldsymbol{\sigma}} = \frac{1}{|\mathcal{V}|} sym\left(\int_{\mathcal{V}} \boldsymbol{\sigma}\, dV\right) \tag{1.8}$$

Taking into account the equilibrium of the RVE (1.1) (assuming $\ddot{\boldsymbol{u}} = \mathbf{0}$) and the identity $\nabla \boldsymbol{x} = I$, and making use of the divergence theorem, we have:

$$\boldsymbol{\sigma} = (\operatorname{div}\boldsymbol{\sigma}) \otimes \boldsymbol{x} + \boldsymbol{\sigma} \cdot (\nabla \boldsymbol{x})^T = \operatorname{div}(\boldsymbol{\sigma} \otimes \boldsymbol{x}) \tag{1.9}$$

Substitution of 1.9 into 1.8, and application of the divergence theorem yields:

$$\bar{\boldsymbol{\sigma}} = \frac{1}{|\mathcal{V}|} sym\left(\int_{\mathcal{V}} \operatorname{div}(\boldsymbol{\sigma} \otimes \boldsymbol{x})\, dV\right) = \frac{1}{|\mathcal{V}|} sym\left(\int_{\partial\mathcal{V}} \boldsymbol{\sigma} \cdot \boldsymbol{n} \otimes \boldsymbol{x}\, dA\right) \Leftrightarrow$$
$$\boxed{\bar{\boldsymbol{\sigma}} = \frac{1}{|\mathcal{V}|}\int_{\partial\mathcal{V}} sym(\boldsymbol{t} \otimes \boldsymbol{x}) dA} \tag{1.10}$$

1.5.3 Internal Work

The energy averaging theorem, known in the literature as the Hill-Mandel condition or macrohomogeneity condition (Hill (1963); Suquet (1985)), requires that the macroscopic volume average of the variation of work performed on the RVE is equal to the local variation of the work on the macroscale. That is:

$$\overline{\boldsymbol{\sigma}}: \dot{\overline{\boldsymbol{\varepsilon}}} = \frac{1}{|\mathcal{V}|}\int_{\mathcal{V}} \boldsymbol{\sigma}: \dot{\boldsymbol{\varepsilon}}\, dV \tag{1.11}$$

It is:

$$\begin{aligned} \boldsymbol{\sigma}: \dot{\boldsymbol{\varepsilon}} = \boldsymbol{\sigma}: sym(\nabla \dot{\boldsymbol{u}}) &\overset{\sigma^T=\sigma}{=} sym(\boldsymbol{\sigma}: \nabla \dot{\boldsymbol{u}}) \\ &= sym[\mathrm{div}(\dot{\boldsymbol{u}} \cdot \boldsymbol{\sigma}) - \mathrm{div}\,\boldsymbol{\sigma} \cdot \dot{\boldsymbol{u}}] \overset{1.1}{=} sym[\mathrm{div}(\dot{\boldsymbol{u}} \cdot \boldsymbol{\sigma})] \end{aligned} \tag{1.12}$$

Substituting 1.12 into 1.11 and applying the divergence theorem, we get:

$$\overline{\boldsymbol{\sigma}}: \dot{\overline{\boldsymbol{\varepsilon}}} = \frac{1}{|\mathcal{V}|}\int_{\mathcal{V}} sym[\mathrm{div}(\dot{\boldsymbol{u}} \cdot \boldsymbol{\sigma})]\, dV = \frac{1}{|\mathcal{V}|}\int_{\partial\mathcal{V}} sym[\dot{\boldsymbol{u}} \cdot \boldsymbol{\sigma} \cdot \boldsymbol{n}] dA = \frac{1}{|\mathcal{V}|}\int_{\partial\mathcal{V}} sym[\dot{\boldsymbol{u}} \cdot \boldsymbol{t}] dA \Leftrightarrow$$

$$\boxed{\overline{\boldsymbol{\sigma}}: \dot{\overline{\boldsymbol{\varepsilon}}} = \frac{1}{|\mathcal{V}|}\int_{\partial\mathcal{V}} \boldsymbol{t} \cdot \dot{\boldsymbol{u}} dA} \tag{1.13}$$

The sensitivity of the macroscopic stress $\overline{\boldsymbol{\sigma}}$ with respect to the macroscopic strain $\dot{\overline{\boldsymbol{\varepsilon}}}$ is determined by the overall tangent moduli $\overline{\mathbb{C}}(t)$. In elasticity, we may write

$$\dot{\overline{\boldsymbol{\sigma}}} = \overline{\mathbb{C}}: \dot{\overline{\boldsymbol{\varepsilon}}} \quad \text{with} \quad \overline{\mathbb{C}} \coloneqq \partial_{\overline{\boldsymbol{\varepsilon}}} \overline{\boldsymbol{\sigma}} \tag{1.14}$$

1.6 Definition of the boundary conditions for the microstructure (Miehe & Koch, 2002)

The boundary conditions for the displacement $\boldsymbol{u}$ and the traction $\boldsymbol{t}$ on the microstructure are chosen in a way that the conditions 1.7,1.10 and 1.13 are a priori satisfied. At first we assume equilibrium for the interior of the RV, i.e.

$$\boldsymbol{t}(\boldsymbol{x},t) = \boldsymbol{0} \;\text{ at }\; \boldsymbol{x} \in \partial\mathcal{H} \tag{1.15}$$

The boundary conditions on the remaining part $\partial\mathcal{V}$, i.e. the surface of the RV, must be related to given macroscopic overall variables. We investigate two variations: (i) linear displacements and (ii) periodicity conditions.
The above formulations belong to the so-called deformation-driven methods. That is, the macroscopic strains $\bar{\boldsymbol{\varepsilon}}(t)$ are prescribed and the macroscopic overall stresses $\bar{\boldsymbol{\sigma}}$ are computed. Thus, all boundary conditions mentioned above must be formulated in terms of the displacement field $\mathbf{u}$ and the given macroscopic strain mode $\bar{\boldsymbol{\varepsilon}}(t)$.

1.6.1 Linear Boundary Constraints

The definition of deformation boundary constraints in terms of the macroscopic strain $\bar{\boldsymbol{\varepsilon}}$ assumes the form

$$\boldsymbol{u}(\boldsymbol{x},t) = \bar{\boldsymbol{\varepsilon}}(t)\boldsymbol{x} \;\text{ at }\; \boldsymbol{x} \in \partial\mathcal{V}, \tag{1.16}$$

This condition defines a linear deformation on the boundary $\partial\mathcal{V}$ of the RV.

We are promptly going to prove that 1.16 satisfies the averaging theorems.

Insertion of 1.16 into 1.7 yields:

$$\begin{aligned}\bar{\boldsymbol{\varepsilon}} &= \frac{1}{|\mathcal{V}|}\int_{\partial\mathcal{V}} sym[\bar{\boldsymbol{\varepsilon}}(t)\boldsymbol{x}\otimes\mathbf{n}]\,dA \overset{\bar{\boldsymbol{\varepsilon}}^T=\bar{\boldsymbol{\varepsilon}}}{=} \frac{1}{|\mathcal{V}|}\bar{\boldsymbol{\varepsilon}}(t)\int_{\partial\mathcal{V}} sym[\boldsymbol{x}\otimes\mathbf{n}]\,dA \\ &= \frac{1}{|\mathcal{V}|}\bar{\boldsymbol{\varepsilon}}(t)\int_{\mathcal{V}} sym[\nabla\boldsymbol{x}]\,dV \overset{\nabla x=I}{=} \bar{\boldsymbol{\varepsilon}}(t)\end{aligned} \tag{1.17}$$

Insertion of 1.16 into 1.13 yields:

$$\begin{aligned}\bar{\boldsymbol{\sigma}}:\dot{\bar{\boldsymbol{\varepsilon}}} &= \frac{1}{|\mathcal{V}|}\int_{\partial\mathcal{V}} \boldsymbol{t}\cdot\dot{\bar{\boldsymbol{\varepsilon}}}(t)\boldsymbol{x}\,dA \\ &= \frac{1}{|\mathcal{V}|}\int_{\partial\mathcal{V}} sym(\,\boldsymbol{t}\cdot\dot{\bar{\boldsymbol{\varepsilon}}}(t)\boldsymbol{x})\,dA \overset{\bar{\boldsymbol{\varepsilon}}^T=\bar{\boldsymbol{\varepsilon}}}{=} \frac{1}{|\mathcal{V}|}\dot{\bar{\boldsymbol{\varepsilon}}}(t):\int_{\partial\mathcal{V}} sym(\boldsymbol{t}\otimes\boldsymbol{x})\,dA\end{aligned} \tag{1.18}$$

Taking into account that the average macroscopic stresses are calculated from 1.10, 1.18 yields:

$$\bar{\boldsymbol{\sigma}}:\dot{\bar{\boldsymbol{\varepsilon}}} = \dot{\bar{\boldsymbol{\varepsilon}}}:\bar{\boldsymbol{\sigma}} \tag{1.19}$$

1.6.2 Periodic deformation and antiperiodic tractions on the boundary

A second possibility to a priori satisfy the averaging theorems is to assume the periodicity conditions

$$\boldsymbol{u}(\boldsymbol{x}^+,t)-\boldsymbol{u}(\boldsymbol{x}^-,t)=\bar{\boldsymbol{\varepsilon}}(t)(\boldsymbol{x}^+-\boldsymbol{x}^-) \quad \text{and} \quad \boldsymbol{t}(\boldsymbol{x}^+,t)+\boldsymbol{t}(\boldsymbol{x}^-,t)=\boldsymbol{0} \quad , \tag{1.20}$$

representing periodic deformations and antiperiodic tractions on the boundary of the RV. Here, the boundary is decomposed into two parts $\partial\mathcal{V}=\partial\mathcal{V}^-\cup\partial\mathcal{V}^+$ with outward normals $\boldsymbol{n}^-=-\boldsymbol{n}^+$ at associated points $\boldsymbol{x}^-\in\partial\mathcal{V}^-$ and $\boldsymbol{x}^+\in\partial\mathcal{V}^+$, respectively.

Next, we are going to prove that 1.20 satisfies the averaging theorems.

We can rewrite 1.20 as:

$$[\![\boldsymbol{u}]\!](\boldsymbol{x},t)=\bar{\boldsymbol{\varepsilon}}(t)[\![\boldsymbol{x}]\!] \quad , \tag{1.21}$$

where $[\![\bullet]\!]:=(\bullet)^+-(\bullet)^-$ is defined at point $\boldsymbol{x}\in\partial\mathcal{V}$.

Eq. 1.7, taking into consideration Eq.1.20 and 1.21 yields:

$$\begin{aligned}
\bar{\boldsymbol{\varepsilon}} &= \frac{1}{|\mathcal{V}|}\left\{\int_{\partial\mathcal{V}^+} sym[\mathbf{u}^+\otimes\mathbf{n}^+]\,dA+\int_{\partial\mathcal{V}^-} sym[\mathbf{u}^-\otimes\mathbf{n}^-]\,dA\right\} \overset{\boldsymbol{n}^-=-\boldsymbol{n}^+}{=} \\
&= \frac{1}{|\mathcal{V}|}\left\{\int_{\partial\mathcal{V}^+} sym[\mathbf{u}^+\otimes\mathbf{n}^+]\,dA-\int_{\partial\mathcal{V}^+} sym[\mathbf{u}^-\otimes\mathbf{n}^+]\,dA\right\} \\
&= \frac{1}{|\mathcal{V}|}\int_{\partial\mathcal{V}^+} sym[[\![\mathbf{u}]\!]\otimes\mathbf{n}^+]\,dA=\frac{1}{|\mathcal{V}|}\int_{\partial\mathcal{V}^+} sym[\bar{\boldsymbol{\varepsilon}}(t)[\![\boldsymbol{x}]\!]\otimes\mathbf{n}^+]\,dA \\
&= \frac{1}{|\mathcal{V}|}\left\{\int_{\partial\mathcal{V}^+} sym[\bar{\boldsymbol{\varepsilon}}(t)\boldsymbol{x}^+\otimes\mathbf{n}^+]\,dA-\int_{\partial\mathcal{V}^+} sym[\bar{\boldsymbol{\varepsilon}}(t)\boldsymbol{x}^-\otimes\mathbf{n}^+]\,dA\right\} \\
&\overset{\boldsymbol{n}^-=-\boldsymbol{n}^+}{=} \frac{1}{|\mathcal{V}|}\int_{\partial\mathcal{V}} sym[\bar{\boldsymbol{\varepsilon}}(t)\boldsymbol{x}\otimes\mathbf{n}]\,dA=\frac{1}{|\mathcal{V}|}\bar{\boldsymbol{\varepsilon}}(t)\int_{\mathcal{V}} sym[\nabla\boldsymbol{x}]\,dV \overset{\nabla\boldsymbol{x}=I}{=} \bar{\boldsymbol{\varepsilon}}(t)
\end{aligned} \tag{1.22}$$

Insertion of 1.16 into 1.13 yields:

$$\begin{aligned}
\bar{\boldsymbol{\sigma}}:\dot{\bar{\boldsymbol{\varepsilon}}} &= \frac{1}{|\mathcal{V}|}\int_{\partial\mathcal{V}}\boldsymbol{t}\cdot\dot{\boldsymbol{u}}dA=\frac{1}{|\mathcal{V}|}sym\left\{\int_{\partial\mathcal{V}}\boldsymbol{t}\cdot\dot{\boldsymbol{u}}dA\right\} \\
&= \frac{1}{|\mathcal{V}|}sym\left\{\int_{\partial\mathcal{V}^+}\boldsymbol{t}^+\cdot\dot{\boldsymbol{u}}^+dA+\int_{\partial\mathcal{V}^-}\boldsymbol{t}^-\cdot\dot{\boldsymbol{u}}^-dA\right\} \\
&\overset{1.20b}{=} \frac{1}{|\mathcal{V}|}sym\left\{\int_{\partial\mathcal{V}^+}\boldsymbol{t}^+\cdot\dot{\boldsymbol{u}}^+dA-\int_{\partial\mathcal{V}^-}\boldsymbol{t}^+\cdot\dot{\boldsymbol{u}}^-dA\right\}
\end{aligned}$$

$$= \frac{1}{|\mathcal{V}|} sym\left\{\int_{\partial\mathcal{V}^+} \boldsymbol{t}^+ \cdot \dot{\boldsymbol{u}}^+ dA - \int_{\partial\mathcal{V}^+} \boldsymbol{t}^+ \cdot \dot{\boldsymbol{u}}^- dA\right\}$$
$$= \frac{1}{|\mathcal{V}|} sym\left\{\int_{\partial\mathcal{V}^+} \boldsymbol{t}^+ \cdot (\dot{\boldsymbol{u}}^+ - \dot{\boldsymbol{u}}^-) dA\right\} \overset{1.20a}{=} \frac{1}{|\mathcal{V}|} sym\left\{\int_{\partial\mathcal{V}^+} \boldsymbol{t}^+ \cdot \dot{\bar{\boldsymbol{\varepsilon}}}(t)(\boldsymbol{x}^+ - \boldsymbol{x}^-) dA\right\}$$

$$= \frac{1}{|\mathcal{V}|} \dot{\bar{\boldsymbol{\varepsilon}}}(t) : sym\left\{\int_{\partial\mathcal{V}^+} \boldsymbol{t}^+ \otimes (\boldsymbol{x}^+ - \boldsymbol{x}^-) dA\right\}$$
$$= \frac{1}{|\mathcal{V}|} \dot{\bar{\boldsymbol{\varepsilon}}}(t) : sym\left\{\int_{\partial\mathcal{V}^+} \boldsymbol{t}^+ \otimes \boldsymbol{x}^+ dA - \int_{\partial\mathcal{V}^+} \boldsymbol{t}^+ \otimes \boldsymbol{x}^- dA\right\}$$
$$\overset{1.20b}{=} \frac{1}{|\mathcal{V}|} \dot{\bar{\boldsymbol{\varepsilon}}}(t) : \int_{\partial\mathcal{V}} sym[\, \boldsymbol{t} \otimes \boldsymbol{x}] dA \qquad 1.23$$

Taking into account that the average macroscopic stresses are calculated from 1.10, 1.23 yields:

$$\bar{\boldsymbol{\sigma}} : \dot{\bar{\boldsymbol{\varepsilon}}} = \dot{\bar{\boldsymbol{\varepsilon}}} : \bar{\boldsymbol{\sigma}} \qquad 1.24$$

1.7 Discretized micro-to-macro-transitions at small strains (Miehe & Koch, 2002)

1.7.1 Discretized microequilibrium state

Let us consider a two-dimensional ($n_{\text{dim}} = 2$) discretized macrostructure, whose microstructure is also discretized in terms of a mesh with N nodal points, see Figure 1-4 and Figure 1-5.

Furthermore, we assume a time discretization of a dynamic problem with possibly time-dependent local constitutive equations. Then the discrete counterpart to the continuous form 1.1 of the microequilibrium in the time increment under consideration may be expressed in terms of the nonlinear mapping

$$\boldsymbol{u} \mapsto \boldsymbol{f}(\boldsymbol{u}) \text{ with } \boldsymbol{u}, \boldsymbol{f} \in \mathcal{R}^{N \cdot n_{\text{dim}}} \tag{1.25}$$

of the global nodal displacement vector $\boldsymbol{u} \in \mathcal{R}^{N \cdot n_{\text{dim}}}$ onto the global *internal nodal force vector* $\boldsymbol{f} \in \mathcal{R}^{N \cdot n_{\text{dim}}}$ at the current discrete time $t \in \mathcal{R}$. The nonlinear functional dependence on the current nodal forces in terms of the current nodal displacements of the FE mesh reflects a particular form of the discretization in time and space. The sensitivity of the internal forces with respect to a change in the nodal displacements is assumed to be governed by the mapping

$$\boldsymbol{u} \mapsto \boldsymbol{K}(\boldsymbol{u}) \coloneqq \partial_{\boldsymbol{u}} \boldsymbol{f}(\boldsymbol{u}) \text{ with } \boldsymbol{K} \in \mathcal{R}^{N \cdot n_{\text{dim}}} \times \mathcal{R}^{N \cdot n_{\text{dim}}} \tag{1.26}$$

Here, $\boldsymbol{K}$ denotes the tangent matrix associated with the internal forces of the discretized structural model. Note that the internal force vector $\boldsymbol{f}$ and the tangent matrix $\boldsymbol{K}$ are considered to be standard elements of computational structural models.

1.7.2 Partitioning of the nonlinear algebraic equations

The nodes of the mesh are partitioned into those on the surface $\partial\mathcal{V}$ the RV and those in the interior of $\mathcal{V}$. Assume that M < N nodes of the mesh lie on the boundary $\partial\mathcal{V}$ as indicated in Figure 1-6. We then consider the partitions of the current nodal positions and internal nodal forces

$$\boldsymbol{u} = \begin{bmatrix} \boldsymbol{u}_a \\ \boldsymbol{u}_b \end{bmatrix} \coloneqq \begin{bmatrix} \mathbb{P}_a \boldsymbol{u} \\ \mathbb{P}_b \boldsymbol{u} \end{bmatrix} \text{ and } \boldsymbol{f} \coloneqq \begin{bmatrix} \mathbb{P}_a \boldsymbol{f} \\ \mathbb{P}_b \boldsymbol{f} \end{bmatrix} \tag{1.27}$$

Here,

$$\mathbb{P}_a \in \mathcal{R}^{(N-M) \cdot n_{\text{dim}}} \times \mathcal{R}^{N \cdot n_{\text{dim}}} \text{ and } \mathbb{P}_b \in \mathcal{R}^{M \cdot n_{\text{dim}}} \times \mathcal{R}^{N \cdot n_{\text{dim}}} \tag{1.28}$$

Are Boolean matrices which project the vector of the global nodes to the vector of the internal nodes and the nodes on the boundary respectively. In line with 1.27, the tangent matrix defined in 1.26 is partitioned

$$\boldsymbol{K} = \begin{bmatrix} \boldsymbol{K}_{aa} & \boldsymbol{K}_{ab} \\ \boldsymbol{K}_{ba} & \boldsymbol{K}_{bb} \end{bmatrix} \coloneqq \begin{bmatrix} \mathbb{P}_a \boldsymbol{K} \mathbb{P}_a^T & \mathbb{P}_a \boldsymbol{K} \mathbb{P}_b^T \\ \mathbb{P}_b \boldsymbol{K} \mathbb{P}_a^T & \mathbb{P}_b \boldsymbol{K} \mathbb{P}_b^T \end{bmatrix} \tag{1.29}$$

into submatrices associated with interior nodes and nodes on the surface of the RV.

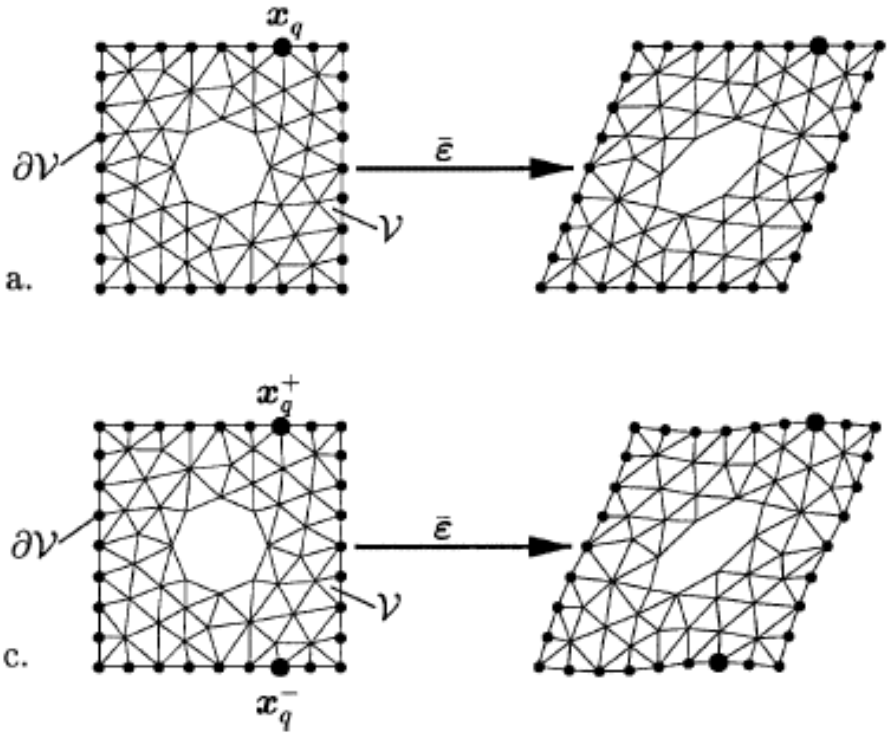

Figure 1-6
Partitioning of nodes and definition of deformation–driven boundary constraints of discretized microstructures. (Miehe & Koch, 2002)

- **a. prescribed deformation $u_q = \bar{\varepsilon} x_q$ for $q = 1 \dots M$ nodes on boundary;**
- **c. Periodic deformation constraint $u_q^+ - u_q^- = \bar{\varepsilon}(x_q^+ - x_q^-)$ for $q = 1 \dots P$ corresponding node pairs on boundary**

1.7.3 Linear displacements on the boundary

We start with the case of the prescribed linear displacements on the boundary $\partial\mathcal{V}$ of the RV. At each node q of this boundary, condition 1.16 induces the discrete constraint

$$\boldsymbol{u_q} = \bar{\boldsymbol{\varepsilon}}(t)\boldsymbol{x_q}, \quad \text{q=1...M} \tag{1.30}$$

in terms of the prescribed macroscopic strain $\bar{\boldsymbol{\varepsilon}}$. Transcribing the strain tensor $\bar{\boldsymbol{\varepsilon}}$ into vector form, and taking the discretization into consideration, we may express $\boldsymbol{u_q}$ and $\bar{\boldsymbol{\varepsilon}}$ in the form:

$$\bar{\boldsymbol{\varepsilon}} \coloneqq [\bar{\varepsilon}_{11} \quad \bar{\varepsilon}_{22} \quad 2\bar{\varepsilon}_{12}]^T \quad \text{and} \quad \boldsymbol{u_q} \coloneqq [u_1 \quad u_2]_q^T \tag{1.31}$$

For $n_{\text{dim}} = 2$, we may rewrite 1.30 as:

$$\boldsymbol{u_q} = \mathbb{D}_q^T \bar{\boldsymbol{\varepsilon}}, \quad \text{q=1...M}\,, \tag{1.32}$$

where $\mathbb{D}_q \in \boldsymbol{\mathcal{R}^3} \times \boldsymbol{\mathcal{R}^2}$ is a matrix that depends on the coordinates of the nodal point q in the reference configuration, for example

$$\mathbb{D}_q \coloneqq \frac{1}{2}\begin{bmatrix} 2x_1 & 0 \\ 0 & 2x_2 \\ x_2 & x_1 \end{bmatrix}_q, \tag{1.33}$$

in the case of $n_{\mathrm{dim}} = 2$. Now define a global coordinate matrix $\mathbb{D} \in \boldsymbol{\mathcal{R}^3} \times \boldsymbol{\mathcal{R}^{2 \cdot M}}$ associated with all M nodes on the surface of the discretized microstructure as

$$\mathbb{D} \coloneqq [\mathbb{D}_1 \quad \mathbb{D}_2 \quad \dots \quad \mathbb{D}_M]. \tag{1.34}$$

Then we may rewrite the constraint 1.16 for the linear displacements on the boundary in the compact global form

$$\boldsymbol{d}(\boldsymbol{u_b}; \bar{\boldsymbol{\varepsilon}}) = \boldsymbol{u_b} - \mathbb{D}^T \bar{\boldsymbol{\varepsilon}} = \boldsymbol{0} \tag{1.35}$$

Applying the Lagrange multiplier method for the incorporation of this constraint in the analysis, we end up with the following set of nonlinear algebraic equations

$$\begin{aligned} \boldsymbol{f_a}(\boldsymbol{x}) &= \boldsymbol{0} \\ \boldsymbol{f_b}(\boldsymbol{x}) - \boldsymbol{\delta} &= \boldsymbol{0} \\ \boldsymbol{u_b} - \mathbb{D}^T \bar{\boldsymbol{\varepsilon}} &= \boldsymbol{0} \end{aligned} \tag{1.36}$$

The system determines the displacements at the discrete time under consideration. The Lagrangian multiplier $\boldsymbol{\delta} \in \boldsymbol{\mathcal{R}^{M \cdot n_{\mathrm{dim}}}}$ represents the external forces on the nodes of the boundary which enforce the constraint 1.35. A Newton-type solution of the nonlinear system of the variable vector $\{\boldsymbol{u} \quad \boldsymbol{\delta}\}$ is based on the linearization

$$\begin{aligned} \boldsymbol{f_a}(\boldsymbol{x}) + \boldsymbol{K_{aa}} \Delta \boldsymbol{u_a} + \boldsymbol{K_{ab}} \Delta \boldsymbol{u_b} &= \boldsymbol{0} \\ \boldsymbol{f_b}(\boldsymbol{x}) - \boldsymbol{\delta} + \boldsymbol{K_{ba}} \Delta \boldsymbol{u_a} + \boldsymbol{K_{bb}} \Delta \boldsymbol{u_b} - \Delta \boldsymbol{\delta} &= \boldsymbol{0} \\ \boldsymbol{u_b} - \mathbb{D}^T \bar{\boldsymbol{\varepsilon}} + \Delta \boldsymbol{u_b} - \mathbb{D}^T \Delta \bar{\boldsymbol{\varepsilon}} &= \boldsymbol{0} \end{aligned} \tag{1.37}$$

The solution is obtained in the following steps. In a typical iteration step at given displacements $\boldsymbol{u_b}$on the surface, i.e. $\Delta \boldsymbol{u_b} = \boldsymbol{0}$, associated with a certain imposed macroscopic deformation $\bar{\boldsymbol{\varepsilon}}$, i.e. $\Delta \bar{\boldsymbol{\varepsilon}} = \boldsymbol{0}$, we use Eq.1.37_1 for the iterative update of the displacements of the internal nodes

$$\boldsymbol{u_a} \Leftarrow \boldsymbol{u_a} + \Delta \boldsymbol{u_a} \quad , \Delta \boldsymbol{u_a} = \boldsymbol{K_{aa}^{-1}} \boldsymbol{f_a} \tag{1.38}$$

The Newton iterations are performed until convergence is obtained , that is, until $\left| |\boldsymbol{f_a}| \right| < tol$. For a known displacement of the microstructure, the forces on the surface are computed from 1.37_2 by

$$\boldsymbol{\delta} = \boldsymbol{f_b}(\boldsymbol{u}). \tag{1.39}$$

In the discrete setting, we consider the limit $\boldsymbol{t} dA \rightarrow \boldsymbol{\delta_q}$ of the infinitesimal force $\boldsymbol{t} dA$ in 1.10 to the finite force $\boldsymbol{\delta_q}$ at the position $\boldsymbol{x_q}$of the node q on the surface of the RV. Then 1.10 degenerates to the discrete sum

$$\bar{\boldsymbol{\sigma}} = \frac{1}{|\mathcal{V}|} \sum_{q=1}^{M} sym[\boldsymbol{\delta_q} \otimes \boldsymbol{x_q}] \tag{1.40}$$

Introducing a matrix representation of the stresses $\bar{\boldsymbol{\sigma}} \in \boldsymbol{\mathcal{R}^3}$ and the nodal forces $\boldsymbol{\delta_q} \in \boldsymbol{\mathcal{R}^2}$, for $n_{\mathrm{dim}} = 2$,

$$\bar{\boldsymbol{\sigma}} \coloneqq [\bar{\boldsymbol{\sigma}}_{\boldsymbol{11}} \quad \bar{\boldsymbol{\sigma}}_{\boldsymbol{22}} \quad \bar{\boldsymbol{\sigma}}_{\boldsymbol{12}}]^{\boldsymbol{T}} \text{ and } \boldsymbol{\delta}_{\boldsymbol{q}} \coloneqq [\boldsymbol{\delta}_{\boldsymbol{1}} \quad \boldsymbol{\delta}_{\boldsymbol{2}}]_{\boldsymbol{q}}^{\boldsymbol{T}} \tag{1.41}$$

We may represent 1.40 in the form:

$$\bar{\boldsymbol{\sigma}} = \frac{1}{|\mathcal{V}|} \sum_{q=1}^{M} \mathbb{D}_{\boldsymbol{q}} \boldsymbol{\delta}_{\boldsymbol{q}} \tag{1.42}$$

with the matrix $\mathbb{D}_{\boldsymbol{q}}$ introduced above. Using the global coordinate matrix $\mathbb{D}$ defined in 1.34, we finally get the macrostress from the global expression

$$\bar{\boldsymbol{\sigma}} = \frac{1}{|\mathcal{V}|} \mathbb{D} \boldsymbol{\delta} \tag{1.43}$$

The sensitivity $\bar{\mathbb{C}} \coloneqq \partial_{\bar{\boldsymbol{\varepsilon}}} \bar{\boldsymbol{\sigma}}$ of the macroscopic stresses with respect to the macroscopic deformation is obtained as follows. The stress sensitivity can be written in the form

$$\Delta \bar{\boldsymbol{\sigma}} = \frac{1}{|\mathcal{V}|} \mathbb{D} \Delta \boldsymbol{\delta} \tag{1.44}$$

Assume a microscopic equilibrium state where 1.36 is satisfied. Then we get from 1.37_1 and 1.37_3 the increments

$$\Delta \boldsymbol{u}_{\boldsymbol{a}} = -\boldsymbol{K}_{\boldsymbol{aa}}^{-\boldsymbol{1}} \boldsymbol{K}_{\boldsymbol{ab}} \Delta \boldsymbol{u}_{\boldsymbol{b}}, \quad \Delta \boldsymbol{u}_{\boldsymbol{b}} = \mathbb{D}^{\boldsymbol{T}} \Delta \bar{\boldsymbol{\varepsilon}} \tag{1.45}$$

Equation 1.37_2 then determines the increment of the forces on the surface

$$\Delta \boldsymbol{\delta} = \widetilde{\boldsymbol{K}}_{\boldsymbol{bb}} \mathbb{D}^{\boldsymbol{T}} \Delta \bar{\boldsymbol{\varepsilon}} \quad \text{with } \widetilde{\boldsymbol{K}}_{\boldsymbol{bb}} \coloneqq \boldsymbol{K}_{\boldsymbol{bb}} - \boldsymbol{K}_{\boldsymbol{ba}} \boldsymbol{K}_{\boldsymbol{aa}}^{-\boldsymbol{1}} \boldsymbol{K}_{\boldsymbol{ab}} \tag{1.46}$$

Insertion of this result into 1.44 finally identifies the macroscopic tangent moduli

$$\bar{\mathbb{C}} = \frac{1}{|\mathcal{V}|} \mathbb{D} \, \widetilde{\boldsymbol{K}}_{\boldsymbol{bb}} \mathbb{D}^{\boldsymbol{T}} \tag{1.47}$$

in terms of the condensed stiffness $\widetilde{\boldsymbol{K}}_{\boldsymbol{bb}}$.

Integration with the Line-Search Method: (for details on the Line-Search Method, see Appendix –Line Search Method)

We consider

$$\boldsymbol{F} = \boldsymbol{f_a}(\boldsymbol{u}),\ \ \boldsymbol{t} = \boldsymbol{u_a} \tag{1.48}$$

We denote with

$$\boldsymbol{t_0} = \boldsymbol{u_{a0}} \tag{1.49}$$

the value of $\boldsymbol{u_a}$ at the end of a Newton-Raphson iteration. Then the step $\boldsymbol{l}$ of the next iteration is equal to:

$$\boldsymbol{l} = \Delta \boldsymbol{u_a}\,, \tag{1.50}$$

where $\Delta \boldsymbol{u_a}$ is calculated from the equation 1.38.

Then the check function $r(a)$ can be calculated as:

$$r(a) = \boldsymbol{f_a}(\boldsymbol{u}) \cdot \Delta \boldsymbol{u_a} \tag{1.51}$$

where

$$\boldsymbol{u} = \boldsymbol{u_{a0}} + a \cdot \Delta \boldsymbol{u_a} \tag{1.52}$$

Finally, we consider that the Newton-Raphson iterations have converged, when

$$\big|\,|\boldsymbol{F}|\big| = \big|\,|\boldsymbol{f_a}|\big| < tol. \tag{1.53}$$

1.7.4 Periodic deformation and antiperiodic tractions on the boundary

Implementation of the periodic boundary conditions needs a discretization of constraints on "pairs" of node positions $\boldsymbol{x}_q^+$ and $\boldsymbol{x}_q^-$ associated with the parts $\partial\mathcal{V}^+$ and $\partial\mathcal{V}^-$ of the surface of the microstructure, s. Figure 1-6. To this end, the boundary of the RV is meshed into P nodes. For the quadrilateral-shaped microstructure of Figure 1-6, we have $P = \frac{M}{2} + 1$ associated pairs of nodes on the surface. For each node pair $q = 1 \dots P$, the periodicity condition 1.21, can be written as:

$$[\![\boldsymbol{u}_q]\!] = \bar{\boldsymbol{\varepsilon}}[\![\boldsymbol{x}_q]\!], \quad q = 1 \dots P \tag{1.54}$$

with jump notation $[\![\boldsymbol{x}_q]\!] = \boldsymbol{x}_q^+ - \boldsymbol{x}_q^-$. Using matrix notations 1.31 and 1.33, we may recast these constraints into the form

$$\boldsymbol{u}_q^+ - \boldsymbol{u}_q^- = (\mathbb{D}_q^{+\boldsymbol{T}} - \mathbb{D}_q^{-\boldsymbol{T}})\bar{\boldsymbol{\varepsilon}}, \quad q = 1 \dots P \tag{1.55}$$

or, in the more compact representation,

$$\mathbb{P}_q \boldsymbol{u}_b = \mathbb{Q}_q^{\boldsymbol{T}} \bar{\boldsymbol{\varepsilon}}, \qquad q = 1 \dots P \tag{1.56}$$

We denote the matrix $\mathbb{P}_q$ as a link-topology matrix associated with the node pair q. The entries of this matrix consist of $\{0,1,-1\}$ only. All P constraints can be assembled in the global matrix notation

$$\boldsymbol{p}(\bar{\boldsymbol{u}}; \bar{\boldsymbol{\varepsilon}}) = \mathbb{P}\boldsymbol{u}_b - \mathbb{Q}^{\boldsymbol{T}}\bar{\boldsymbol{\varepsilon}} = \boldsymbol{0} \tag{1.57}$$

with the coordinate matrix $\mathbb{Q} := \mathbb{D}^{+\boldsymbol{T}} - \mathbb{D}^{-\boldsymbol{T}} \in \boldsymbol{\mathcal{R}}^{\boldsymbol{3}} \times \mathcal{R}^{P \cdot n_{\mathrm{dim}}}$ for the case $n_{\mathrm{dim}} = 2$, constructed in analogy to (26). The matrix $\mathbb{P} \in \boldsymbol{\mathcal{R}}^{P \cdot n_{\mathrm{dim}}} \times \mathcal{R}^{M \cdot n_{\mathrm{dim}}}$ is effectively stored as a standard topology array in a FE analysis.

Applying the Lagrange multiplier method for the incorporation of these constraints into the analysis of the microstructure, we have the following set of nonlinear equations:

$$\begin{aligned} &\boldsymbol{f}_a(\boldsymbol{u}) = \boldsymbol{0} \\ &\boldsymbol{f}_b(\boldsymbol{u}) - \mathbb{P}^{\boldsymbol{T}}\boldsymbol{\pi} = \boldsymbol{0} \\ &\mathbb{P}\boldsymbol{u}_b - \mathbb{Q}^{\boldsymbol{T}}\bar{\boldsymbol{\varepsilon}} = \boldsymbol{0} \end{aligned} \tag{1.58}$$

The Lagrangian multiplier $\boldsymbol{\pi} \in \mathcal{R}^{M \cdot n_{\mathrm{dim}}}$ represents the pair of forces acting on the node pairs of the boundary, in order for the constraint of 1.56 to be satisfied. The set 1.58 determines the state of the microstructure, except rigid body motions; we exclude these by adding some artificial constraints. A Newton-type solution of the nonlinear system at $\{\boldsymbol{x}, \boldsymbol{\pi}\}$ is based on the linearization

$$\begin{aligned} &\boldsymbol{f}_a(\boldsymbol{u}) + \boldsymbol{K}_{aa}\Delta\boldsymbol{u}_a + \boldsymbol{K}_{ab}\Delta\boldsymbol{u}_b = \boldsymbol{0} \\ &\boldsymbol{f}_b(\boldsymbol{u}) - \mathbb{P}^{\boldsymbol{T}}\boldsymbol{\pi} + \boldsymbol{K}_{ba}\Delta\boldsymbol{u}_a + \boldsymbol{K}_{bb}\Delta\boldsymbol{u}_b - \mathbb{P}^{\boldsymbol{T}}\Delta\boldsymbol{\pi} = \boldsymbol{0} \\ &\mathbb{P}\boldsymbol{u}_b - \mathbb{Q}^{\boldsymbol{T}}\bar{\boldsymbol{\varepsilon}} + \mathbb{P}\Delta\boldsymbol{u}_b - \mathbb{Q}^{\boldsymbol{T}}\Delta\bar{\boldsymbol{\varepsilon}} = \boldsymbol{0} \end{aligned} \tag{1.59}$$

The solution is obtained in the following steps: Eq. 1.59_1 allows the elimination of the increments $\Delta\boldsymbol{u}_a$ of the nodal positions in the interior domain via

$$\Delta \boldsymbol{u}_{\boldsymbol{a}} = -\boldsymbol{K}_{\boldsymbol{aa}}^{-\mathbf{1}}(\boldsymbol{f}_{\boldsymbol{a}} + \boldsymbol{K}_{\boldsymbol{ab}}\Delta \boldsymbol{u}_{\boldsymbol{b}}), \tag{1.60}$$

and induces the system of equations:

$$\begin{aligned} \tilde{\boldsymbol{f}}_{\boldsymbol{b}} - \mathbb{P}^{\boldsymbol{T}}\boldsymbol{\pi} + \widetilde{\boldsymbol{K}}_{\boldsymbol{bb}}\Delta \boldsymbol{u}_{\boldsymbol{b}} - \mathbb{P}^{\boldsymbol{T}}\Delta \boldsymbol{\pi} &= \mathbf{0} \\ \mathbb{P}\boldsymbol{u}_{\boldsymbol{b}} - \mathbb{Q}^{\boldsymbol{T}}\bar{\boldsymbol{\varepsilon}} + \mathbb{P}\Delta \boldsymbol{u}_{\boldsymbol{b}} - \mathbb{Q}^{\boldsymbol{T}}\Delta \bar{\boldsymbol{\varepsilon}} &= \mathbf{0} \end{aligned} \tag{1.61}$$

in terms of the condensed matrices

$$\begin{aligned} \tilde{\boldsymbol{f}}_{\boldsymbol{b}} &\coloneqq \boldsymbol{f}_{\boldsymbol{b}} - \boldsymbol{K}_{\boldsymbol{ba}}\boldsymbol{K}_{\boldsymbol{aa}}^{-\mathbf{1}}\boldsymbol{f}_{\boldsymbol{a}} \\ \widetilde{\boldsymbol{K}}_{\boldsymbol{bb}} &\coloneqq \boldsymbol{K}_{\boldsymbol{bb}} - \boldsymbol{K}_{\boldsymbol{ba}}\boldsymbol{K}_{\boldsymbol{aa}}^{-\mathbf{1}}\boldsymbol{K}_{\boldsymbol{ab}} \end{aligned} \tag{1.62}$$

From 1.61_1, we obtain the increment of the nodal positions on the boundary of the microstructure

$$\Delta \boldsymbol{u}_{\boldsymbol{b}} = -\widetilde{\boldsymbol{K}}_{\boldsymbol{bb}}^{-\mathbf{1}}[\,\tilde{\boldsymbol{f}}_{\boldsymbol{b}} - \mathbb{P}^{\boldsymbol{T}}\boldsymbol{\pi} - \mathbb{P}^{\boldsymbol{T}}\Delta \boldsymbol{\pi}] \tag{1.63}$$

Insertion into 1.61_2 then yields

$$\Delta \boldsymbol{\pi} = -\left[\mathbb{P}\widetilde{\boldsymbol{K}}_{\boldsymbol{bb}}\mathbb{P}^{\boldsymbol{T}}\right]^{-\mathbf{1}}[\left(\mathbb{P}\boldsymbol{u}_{\boldsymbol{b}} - \mathbb{Q}^{\boldsymbol{T}}\bar{\boldsymbol{\varepsilon}}\right) - \mathbb{P}\widetilde{\boldsymbol{K}}_{\boldsymbol{bb}}^{-\mathbf{1}}(\tilde{\boldsymbol{f}}_{\boldsymbol{b}} - \mathbb{P}^{\boldsymbol{T}}\boldsymbol{\pi}) - \mathbb{Q}^{\boldsymbol{T}}\Delta \bar{\boldsymbol{\varepsilon}}] \tag{1.64}$$

Regularity of the projected matrix $\mathbb{P}\widetilde{\boldsymbol{K}}_{\boldsymbol{bb}}\mathbb{P}^{\boldsymbol{T}}$ is ensured by a mass-type diagonal perturbation. In a typical Newton iteration step at frozen macroscopic deformation $\bar{\boldsymbol{\varepsilon}}$, the increments $\Delta \boldsymbol{\pi}$, $\Delta \boldsymbol{u}_{\boldsymbol{b}}$ and $\Delta \boldsymbol{u}_{\boldsymbol{a}}$ are computed from 1.64,1.63 and 1.60 respectively for $\Delta \bar{\boldsymbol{\varepsilon}} = \mathbf{0}$. The update of the variables is then performed by

$$\begin{aligned} \boldsymbol{\pi} &\Leftarrow \boldsymbol{\pi} + \Delta \boldsymbol{\pi} \\ \boldsymbol{u}_{\boldsymbol{b}} &\Leftarrow \boldsymbol{u}_{\boldsymbol{b}} + \Delta \boldsymbol{u}_{\boldsymbol{b}} \\ \boldsymbol{u}_{\boldsymbol{a}} &\Leftarrow \boldsymbol{u}_{\boldsymbol{a}} + \Delta \boldsymbol{u}_{\boldsymbol{a}} \end{aligned} \tag{1.65}$$

In the discrete setting, we consider the limit $\boldsymbol{t}dA \to \boldsymbol{\pi}_{\boldsymbol{q}}$ of the infinitesimal force $\boldsymbol{t}dA$ in 1.10 to the finite forces $\boldsymbol{\pi}_{\boldsymbol{q}}$ acting on the node pair q associated with the positions $\boldsymbol{x}_{\boldsymbol{q}}^{+}$ and $\boldsymbol{x}_{\boldsymbol{q}}^{-}$, respectively. Then 1.10 degenerates to the discrete sum

$$\bar{\boldsymbol{\sigma}} = \frac{1}{|\mathcal{V}|}\sum_{q=1}^{P} sym\left[\boldsymbol{\pi}_{\boldsymbol{q}} \otimes (\boldsymbol{x}_{\boldsymbol{q}}^{+} - \boldsymbol{x}_{\boldsymbol{q}}^{-})\right] \tag{1.66}$$

Introducing a matrix representation of the stresses $\bar{\boldsymbol{\sigma}} \in \boldsymbol{\mathcal{R}}^{\mathbf{3}}$ and the nodal forces $\boldsymbol{\pi}_{\boldsymbol{q}} \in \boldsymbol{\mathcal{R}}^{\mathbf{2}}$, for $n_{\mathrm{dim}} = 2$, in analogy to 1.41 we may represent 1.66 in the form

$$\bar{\boldsymbol{\sigma}} = \frac{1}{|\mathcal{V}|}\sum_{q=1}^{M} \mathbb{Q}_{\boldsymbol{q}}\boldsymbol{\pi}_{\boldsymbol{q}}, \tag{1.67}$$

with the matrix $\mathbb{Q}_{\boldsymbol{q}}$ introduced above. Using the global coordinate matrix $\mathbb{Q}$ defined in 1.56, we finally get the macrostress by means of the global expression

$$\bar{\boldsymbol{\sigma}} = \frac{1}{|\mathcal{V}|}\mathbb{Q}\boldsymbol{\pi} \tag{1.68}$$

The sensitivity $\bar{\mathbb{C}} \coloneqq \partial_{\bar{\boldsymbol{\varepsilon}}}\bar{\boldsymbol{\sigma}}$ of the macroscopic stresses with respect to the macroscopic deformation is obtained as follows. The stress sensitivity can be written in the form

$$\Delta\bar{\boldsymbol{\sigma}} = \frac{1}{|\mathcal{V}|}\mathbb{Q}\Delta\boldsymbol{\pi} \tag{1.69}$$

Assume a microscopic equilibrium state where 1.58 is satisfied. Then we get from 1.37_1 and 1.37_3 the increments

Then the sensitivity $\Delta\boldsymbol{\pi}$ of the Lagrange parameter with respect to a change in the macroscopic deformation is easily derived from 1.64 and takes the closed form

$$\Delta\boldsymbol{\pi} = \left[\mathbb{P}\widetilde{\boldsymbol{K}}_{\boldsymbol{bb}}\mathbb{P}^{\boldsymbol{T}}\right]^{-\mathbf{1}}\mathbb{Q}^{\boldsymbol{T}}\Delta\bar{\boldsymbol{\varepsilon}} \tag{1.70}$$

Insertion into 1.69 then finally identifies the overall moduli

$$\bar{\boldsymbol{\sigma}} = \frac{1}{|\mathcal{V}|}\mathbb{Q}\left[\mathbb{P}\widetilde{\boldsymbol{K}}_{\boldsymbol{bb}}\mathbb{P}^{\boldsymbol{T}}\right]^{-\mathbf{1}}\mathbb{Q}^{\boldsymbol{T}} \tag{1.71}$$

Integration with the Line-Search Method: (for details on the Line-Search Method, see Appendix –Line Search Method)

We consider

$$\boldsymbol{F} = \begin{Bmatrix} \boldsymbol{f_a(u)} \\ \boldsymbol{f_b(u)} - \mathbb{P}^{\boldsymbol{T}}\boldsymbol{\pi} \\ \mathbb{P}\boldsymbol{u_b} - \mathbb{Q}^{\boldsymbol{T}}\bar{\boldsymbol{\varepsilon}} \end{Bmatrix}, \quad \boldsymbol{t} = \begin{Bmatrix} \boldsymbol{u_a} \\ \boldsymbol{u_b} \\ \boldsymbol{\pi} \end{Bmatrix} \tag{1.72}$$

We denote with

$$\boldsymbol{t_0} = \begin{Bmatrix} \boldsymbol{u_{a0}} \\ \boldsymbol{u_{b0}} \\ \boldsymbol{\pi_0} \end{Bmatrix} \tag{1.73}$$

the values of $\boldsymbol{u_a}, \boldsymbol{u_b}, \boldsymbol{\pi}$ at the end of a Newton-Raphson iteration. Then the step $\boldsymbol{l}$ of the next iteration is equal to:

$$\boldsymbol{l} = \begin{Bmatrix} \Delta\boldsymbol{u_a} \\ \Delta\boldsymbol{u_b} \\ \Delta\boldsymbol{\pi} \end{Bmatrix}, \tag{1.74}$$

where $\Delta\boldsymbol{u_a}, \Delta\boldsymbol{u_b}, \Delta\boldsymbol{\pi}$ are calculated from the equations 1.60, 1.63 and 1.64 respectively.

Then the check function $r(a)$ can be calculated as:

$$r(a) = \begin{Bmatrix} \boldsymbol{f_a(u)} \\ \boldsymbol{f_b(u)} - \mathbb{P}^{\boldsymbol{T}}\boldsymbol{\pi} \\ \mathbb{P}\boldsymbol{u_b} - \mathbb{Q}^{\boldsymbol{T}}\bar{\boldsymbol{\varepsilon}} \end{Bmatrix} \cdot \begin{Bmatrix} \Delta\boldsymbol{u_a} \\ \Delta\boldsymbol{u_b} \\ \Delta\boldsymbol{\pi} \end{Bmatrix} \tag{1.75}$$

where

$$\boldsymbol{u} = \begin{Bmatrix} \boldsymbol{u_{a0}} \\ \boldsymbol{u_{b0}} \end{Bmatrix} + a \cdot \begin{Bmatrix} \Delta\boldsymbol{u_a} \\ \Delta\boldsymbol{u_b} \end{Bmatrix}, \quad \boldsymbol{\pi} = \boldsymbol{\pi_0} + \boldsymbol{a} \cdot \Delta\boldsymbol{\pi} \tag{1.76}$$

Finally, we consider that the Newton-Raphson iterations have converged, when

$$||\boldsymbol{F}|| = \left|\left| \begin{Bmatrix} \boldsymbol{f_a}(\boldsymbol{u}) \\ \boldsymbol{f_b}(\boldsymbol{u}) - \mathbb{P}^{\boldsymbol{T}}\boldsymbol{\pi} \\ \mathbb{P}\boldsymbol{u_b} - \mathbb{Q}^{\boldsymbol{T}}\bar{\boldsymbol{\varepsilon}} \end{Bmatrix} \right|\right| < tol. \tag{1.77}$$

2 Bond-Slip Mathematical Formulation

In this chapter a brief summary of the bond-slip mathematical formulation is presented, as described by (Lykidis & Spiliopoulos, 2008).

Let a fiber element be embedded in a "parent" matrix element, and let u_f be the displacement of the fiber, u_m the displacement of the matrix and s the slippage between the two (see Figure 2-1). Then the fiber element displacement can be derived as the superposition of the matrix element displacement and the slippage, as:

$$u_f = u_m + s \tag{2.1}$$

If l_1, m_1, n_1 are the direction cosines of the fiber, then it is:

$$u_m = \{l_1\ m_1\ n_1\} \cdot \begin{Bmatrix} u_{m,x} \\ u_{m,y} \\ u_{m,z} \end{Bmatrix} \tag{2.2}$$

Strain at any point of the fiber is given by:

$$\varepsilon_f = \frac{du_f}{dl} = \frac{du_m}{dl} + \frac{ds}{dl} = \varepsilon_{m,f} + \frac{ds}{dl} \tag{2.3}$$

We denote with $\boldsymbol{d}$ the parent element's nodal displacement, then the axial strain of the parent element along the fiber element axis is calculated as:

$$\varepsilon_{m,f} = \boldsymbol{T}^* \cdot \boldsymbol{\varepsilon_m} = \boldsymbol{T}^* \cdot \boldsymbol{B_m} \cdot \boldsymbol{d} \tag{2.4}$$

where

$$\boldsymbol{T}^* = \{l_1^2 \quad m_1^2 \quad n_1^2 \quad l_1 \cdot n_1 \quad m_1 \cdot n_1 \quad l_1 \cdot n_1\} \tag{2.5}$$

and $\boldsymbol{B_m}$ are the shape function derivatives for the parent matrix element.

If we assume that the slip field along the fiber is expressed via the truss shape functions $\boldsymbol{N_f}$ and the slip at the truss element's nodal points $\boldsymbol{u_{slip}}$, then it is:

$$s = \boldsymbol{N_f} \cdot \boldsymbol{u_{slip}} \Rightarrow \tag{2.6}$$

$$\frac{ds}{dl} = \frac{d\boldsymbol{N_f}}{dl} \cdot \boldsymbol{u_{slip}} = \boldsymbol{B_f} \cdot \boldsymbol{u_{slip}} \tag{2.7}$$

The strain along the fiber can then be expressed as:

$$\varepsilon_f = [\boldsymbol{T}^* \cdot \boldsymbol{B_m} \quad \boldsymbol{B_f}] \cdot \begin{Bmatrix} \boldsymbol{d} \\ \boldsymbol{u_{slip}} \end{Bmatrix} = \boldsymbol{B}^* \cdot \boldsymbol{d}^* \tag{2.8}$$

Having then achieved equilibrium at step t between the internal forces and the external forces vector $[\boldsymbol{R_t} \quad \boldsymbol{P_t}]^T$, where $\boldsymbol{R_t}$ are the external forces acting upon the matrix nodes, and $\boldsymbol{P_t}$ are the external forces acting upon the slip nodes (e.g. prestressing), the incremental form of the virtual work principle between step t and $t + \Delta t$ can be written as:

$$\int_{V_f} \delta\Delta\varepsilon_f * \left(\sigma_f + \Delta\sigma_f\right) dV_f + \int_L \delta\Delta s \cdot (\tau_b + \Delta\tau_b) dL + \int_{V_m} \delta\Delta\boldsymbol{\varepsilon}_{\boldsymbol{m}}^T \cdot (\boldsymbol{\sigma_c} + \boldsymbol{\Delta\sigma_c}) \delta V_m = \delta\boldsymbol{\Delta d}^T \cdot \boldsymbol{R_{t+\Delta t}} + \delta\boldsymbol{\Delta u}_{\boldsymbol{slip}}^T \cdot \boldsymbol{P_{t+\Delta t}} \quad 2.9$$

where V_f, V_m:the fiber and matrix volumes respectively, and L:the external surface area of the fiber.

The incremental stresses can be derived by the tangential constitutive law of the corresponding materials according to the relations:

$$\Delta\boldsymbol{\sigma_m} = \boldsymbol{D_m} \cdot \Delta\boldsymbol{\varepsilon_m},\ \Delta\sigma_f = E_f \cdot \Delta\varepsilon_f,\ \Delta\tau_b = k * \Delta s \quad 2.10$$

If we denote with O_f the fiber section perimeter, with A_f the fiber section area and with l its length, then dV_f, dL can be written as:

$$dV_f = A_f \cdot dl, \quad dL = O_f \cdot dl \quad 2.11$$

Substituting 2.10 and 2.11 in 2.9 we get:

$$\begin{aligned}\int_l [\delta(\boldsymbol{B}^*\boldsymbol{\Delta d}^*)^T \cdot E_f \cdot (\boldsymbol{B}^*\boldsymbol{\Delta d}^*) \cdot A_f + \delta\left(\boldsymbol{N_f}\boldsymbol{\Delta u_{slip}}\right)^T \cdot k \cdot \left(\boldsymbol{N_f}\boldsymbol{\Delta u_{slip}}\right)^T \cdot O_f] dl \\ + \int_l \left[\delta(\boldsymbol{B}^*\boldsymbol{\Delta d}^*)^T \cdot \sigma_f \cdot A_f + \delta\left(\boldsymbol{N_f}\boldsymbol{\Delta u_{slip}}\right)^T \cdot \tau_b \cdot O_f\right] dl \\ + \int_{V_m} \delta(\boldsymbol{B_m} \cdot \boldsymbol{\delta d})^T [\boldsymbol{\sigma_m} + \boldsymbol{D_m} \cdot (\boldsymbol{B_m} \cdot \boldsymbol{\Delta d})] dV_m \\ = \delta\boldsymbol{\Delta d}^T \cdot \boldsymbol{R_{t+\Delta t}} + \delta\boldsymbol{\Delta u}_{\boldsymbol{slip}}^T \cdot \boldsymbol{P_{t+\Delta t}}\end{aligned} \quad 2.12$$

Using Eq. 2.8, and taking into account that Eq. 2.12 holds for any virtual displacement $\{\delta\boldsymbol{\Delta d} \quad \delta\boldsymbol{\Delta u_{slip}}\}^T$, Eq. 2.12 can be re-written as:

$$\left\{\begin{bmatrix} \boldsymbol{K_{mm}} + \boldsymbol{K_{ff,m}} & \boldsymbol{K_{mf}} \\ \boldsymbol{K_{fm}} & \boldsymbol{K_{ff}} + \boldsymbol{K_{bb}} \end{bmatrix} \cdot \begin{Bmatrix} \boldsymbol{\Delta d} \\ \boldsymbol{\Delta u_{slip}} \end{Bmatrix} + \begin{Bmatrix} \boldsymbol{Q_{m,f}} \\ \boldsymbol{Q_b} \end{Bmatrix}\right\} = \begin{Bmatrix} \boldsymbol{R_{t+\Delta t}} \\ \boldsymbol{P_{t+\Delta t}} \end{Bmatrix} \quad 2.13$$

Where:

$$\begin{aligned} \boldsymbol{K_{mm}} &= \int_{V_m} \boldsymbol{B_m^T} \cdot \boldsymbol{D_m} \cdot \boldsymbol{B_m} dV_m \\ \boldsymbol{K_{mm,f}} &= \int_l \boldsymbol{B_m^T} \boldsymbol{T}^{*T} E_f A_f \cdot \boldsymbol{T}^{*T} \boldsymbol{B_m} dl \\ \boldsymbol{K_{mf}} &= \boldsymbol{K_{fm}^T} = \int_l \boldsymbol{B_m^T} \boldsymbol{T}^{*T} E_f A_f \boldsymbol{B_f} dl \end{aligned} \quad 2.14$$

$$\boldsymbol{K_{ff}} = \int_l \boldsymbol{B_f^T} E_f A_f \boldsymbol{B_f} dl \quad \boldsymbol{K_{bb}} = \int_l \boldsymbol{N_f^T} k O_f \boldsymbol{N_f} dl \quad 2.15$$

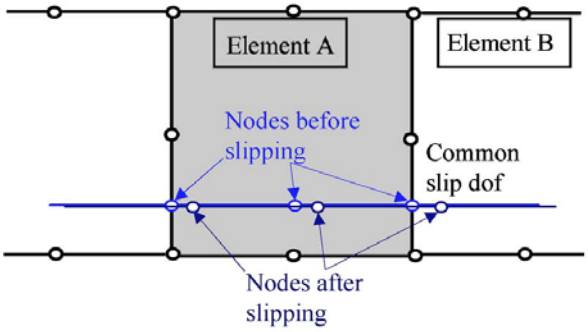

Figure 2-1
(Lykidis & Spiliopoulos, 2008)

$$\boldsymbol{Q_{m,f}} = \int_{V_m} \boldsymbol{B_m^T} \cdot \boldsymbol{\sigma_m} dV_m + \int_l \boldsymbol{B_m^T} \boldsymbol{T^{*T}} \sigma_f A_f dl$$
$$\boldsymbol{Q_b} = \int_l \boldsymbol{B_f^T} \sigma_f A_f dl + \int_l \boldsymbol{N_f^T} \tau_b O_f dl \qquad 2.16$$

If multiple fibers are embedded in the element, then Eq. 2.13 takes the form:

$$\begin{bmatrix} \boldsymbol{K_{mm}} + \sum_{i=1}^{nf} \boldsymbol{K_{ff,m,i}} & \boldsymbol{K_{mf,2}} & \boldsymbol{K_{mf,3}} & \dots & \boldsymbol{K_{mf,i}} & \dots & \boldsymbol{K_{mf,nf}} \\ \boldsymbol{K_{fm,1}} & \boldsymbol{K_{ff,1}} + \boldsymbol{K_{bb,1}} & \boldsymbol{0} & \dots & \boldsymbol{0} & \dots & \boldsymbol{0} \\ \boldsymbol{K_{fm,2}} & \boldsymbol{0} & \boldsymbol{K_{ff,2}} + \boldsymbol{K_{bb,2}} & \dots & \boldsymbol{0} & \dots & \boldsymbol{0} \\ \dots & \dots & \dots & \dots & \dots & \dots & \dots \\ \boldsymbol{K_{fm,i}} & \boldsymbol{0} & \boldsymbol{0} & \dots & \boldsymbol{K_{ff,i}} + \boldsymbol{K_{bb,i}} & \dots & \boldsymbol{0} \\ \dots \dots & \dots & \dots & \dots & \dots & \dots & \dots \\ \boldsymbol{K_{fm,nf}} & \boldsymbol{0} & \boldsymbol{0} & \dots & \boldsymbol{0} & \dots & \boldsymbol{K_{ff,nf}} + \boldsymbol{K_{bb,nf}} \end{bmatrix} \cdot \begin{Bmatrix} \boldsymbol{\Delta d} \\ \boldsymbol{\Delta u_{slip}} \end{Bmatrix} = \begin{Bmatrix} \boldsymbol{R_{t+\Delta t}} - \boldsymbol{Q_{m,f}} \\ \boldsymbol{P_{t+\Delta t}} - \boldsymbol{Q_b} \end{Bmatrix} \qquad 2.17$$

where $\boldsymbol{\Delta u_{slip}}$ is a column vector that includes the slip displacements for all the embedded fibers in the concrete element. These additional slip d.o.f. are common at the interface of two adjacent matrix elements (see Figure 2-1) .For this reason they need to be present in the global structure stiffness matrix as separate d.o.f. and they cannot be condensed after the formation of the local element stiffness matrix. In the case of full bond, Eq. 2.17 becomes:

$$\left[\boldsymbol{K_{mm}} + \left(\sum_{i=1}^{nf} \boldsymbol{K_{ff,m,i}} \right) \right] \cdot \boldsymbol{\Delta d} = \boldsymbol{R_{t+\Delta t}} - \boldsymbol{Q_{m,f}} \qquad 2.18$$

In the case where no fibers are embedded in the element, Eq. 2.17 becomes:

$$\boldsymbol{K_{mm}} \cdot \boldsymbol{\Delta d} = \boldsymbol{R_{t+\Delta t}} - \boldsymbol{Q_{m,f}} \qquad 2.19$$

3 Numerical Examples

3.1 Elastic Modelling

3.1.1 Microscopic Model

We consider a microstructure which consists of a fiber of diameter $d_f = 0.3568$ (cross-section $A_f = 0.1$), made of material with Young's modulus $E_f = 10000$, embedded in a matrix of thickness $t_m = 1$ and made of material with Young's modulus $E_m = 100$ and Poisson's ratio $\nu = 0.2$, which is represented by a RVE shown in Figure 3-1. Full bond between the fiber and the matrix is assumed, that is, no slip is allowed between the two elements. The microstructure is modelled using plane-stress elements for the matrix and truss elements for the fiber, and is analyzed using the Finite Element Method.

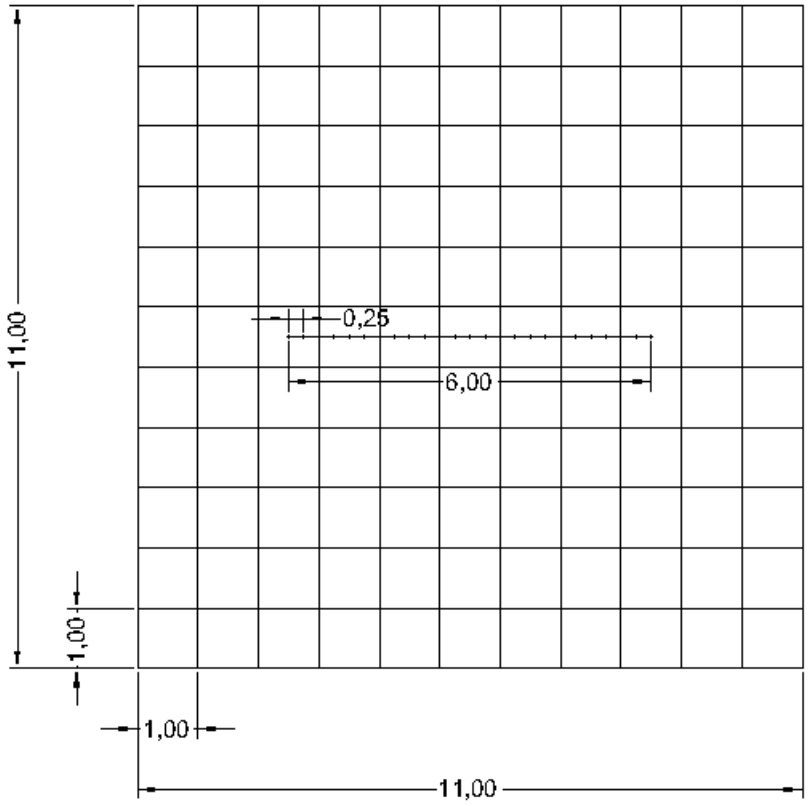

Figure 3-1
RVE configuration

The fiber is discretized into elements of length 0.25, and the matrix is discretized into elements of width 1, as shown in Figure 3-1.

The RVE is then deformed monotonically with strain $\{\varepsilon_{11} \quad \varepsilon_{22} \quad \gamma_{12}\}^T = \{\varepsilon_1 \quad -0.2\varepsilon_1 \quad 0\}^T$, until strain $\varepsilon_1 = 0.05$ is achieved, using the first-order homogenization scheme (linear and periodic prescribed boundary displacements). The results for strain $\varepsilon_1 = 0.05$ are shown below.

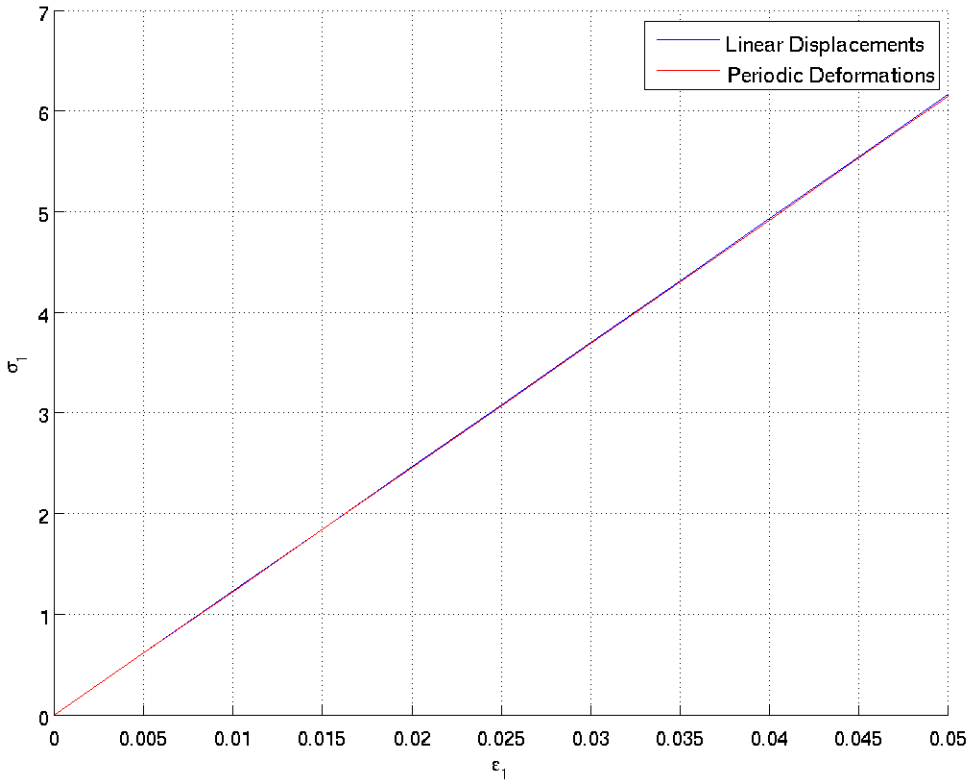

Figure 3-2
Stress-strain curve for x-direction($\sigma_1 - \varepsilon_1$)

Figure 3-2 depicts the variation of stress σ_{11} with strain ε_{11}. The differences between the two homogenization schemes are practically indiscernible.

The elasticity matrices and stresses at $\varepsilon_1 = 0.05$ are equal to:

$$\mathbb{C}_{linear} = \begin{bmatrix} 127.41143 & 20.833333 & -1.6653345E-16 \\ 20.833333 & 104.16667 & 6.2033712E-14 \\ 3.0475622E-14 & 5.012657E-14 & 41.666667 \end{bmatrix}$$

$$\mathbb{C}_{periodic} = \begin{bmatrix} 127.0501 & 20.833333 & -3.375078\mathrm{E}-14 \\ 20.833333 & 104.16667 & -4.911989\mathrm{E}-15 \\ -1.7540482\mathrm{E}-14 & -8.4076571\mathrm{E}-15 & 41.666667 \end{bmatrix}$$

$$\sigma_{linear} = \begin{Bmatrix} 6.162238 \\ -3.1082992E-15 \\ -3.9621084E-15 \end{Bmatrix}$$

$$\sigma_{periodic} = \begin{Bmatrix} 6.1441716 \\ 9.0205621E-17 \\ -1.4084301E-15 \end{Bmatrix}$$

We observe that the elasticity matrix computed from the linear homogenization scheme is slightly larger than the one computed from the periodic homogenization scheme, as expected.

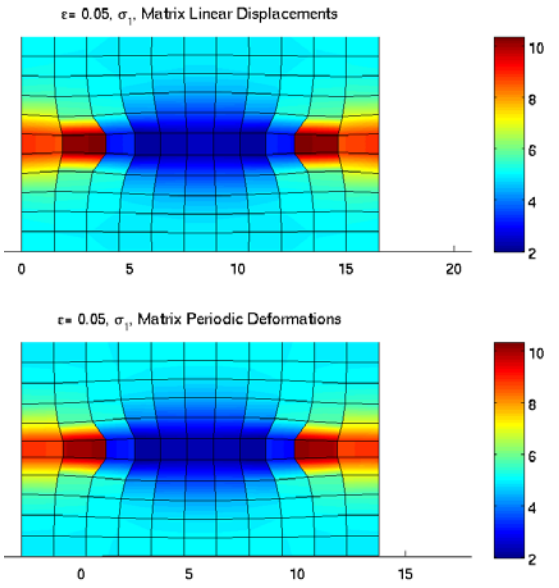

Figure 3-3
Stress σ_{11} for $\varepsilon_1 = 0.05$, Linear and Periodic Prescribed Boundary Deformations

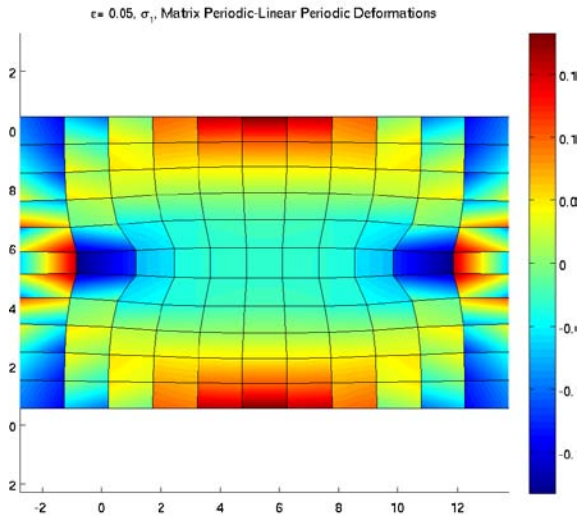

Figure 3-4
Stress σ_{11} for $\varepsilon_1 = 0.05$, Difference between Periodic and Linear Prescribed Boundary Deformations

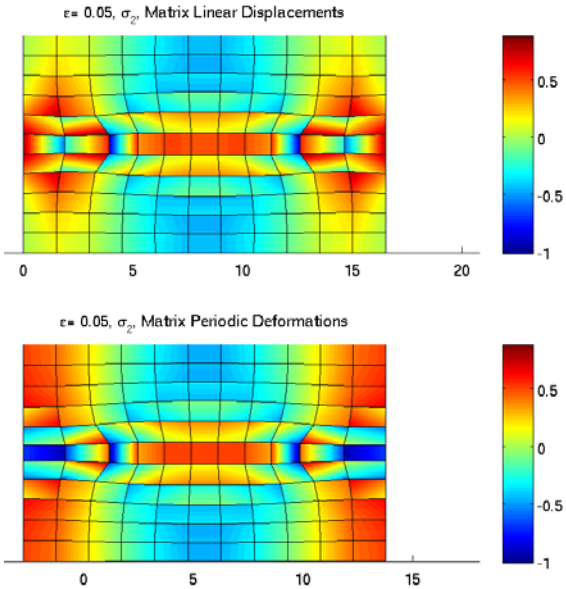

Figure 3-5
Stress σ_{22} for $\varepsilon_1 = 0.05$, Linear and Periodic Prescribed Boundary Deformations

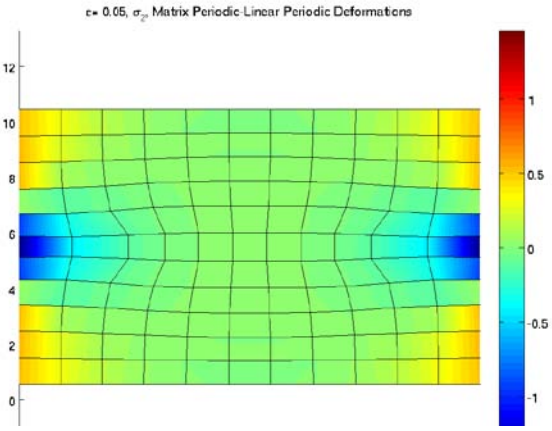

Figure 3-6
Stress σ_{22} for $\varepsilon_1 = 0.05$, Difference between Periodic and Linear Prescribed Boundary Deformations

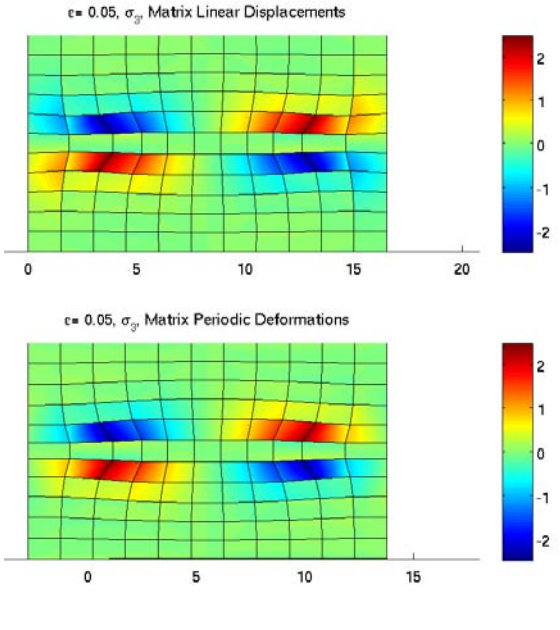

Figure 3-7
Stress τ_{12} for $\varepsilon_1 = 0.05$, Linear and Periodic Prescribed Boundary Deformations

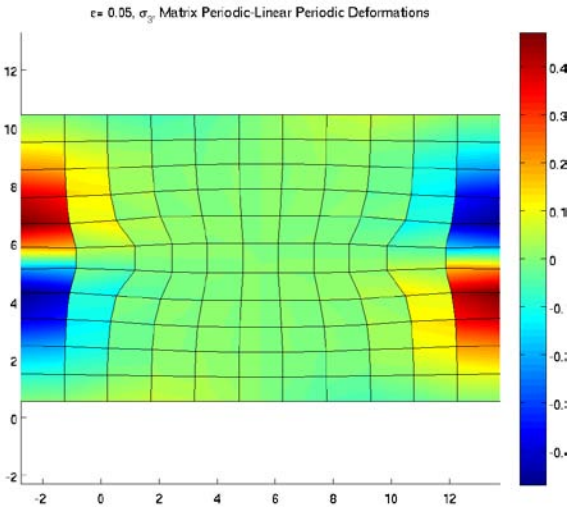

Figure 3-8
Stress τ_{12} for $\varepsilon_1 = 0.05$, Difference between Periodic and Linear Prescribed Boundary Deformations

Figures Figure 3-3 and 3-8 show the stress distribution in the deformed configuration for the linear and periodic prescribed conditions, as well as the variation in stresses between the two. It is observed that the stresses σ_{11} and τ_{12} show the greatest spatial variation. The reason for this will be explained subsequently.

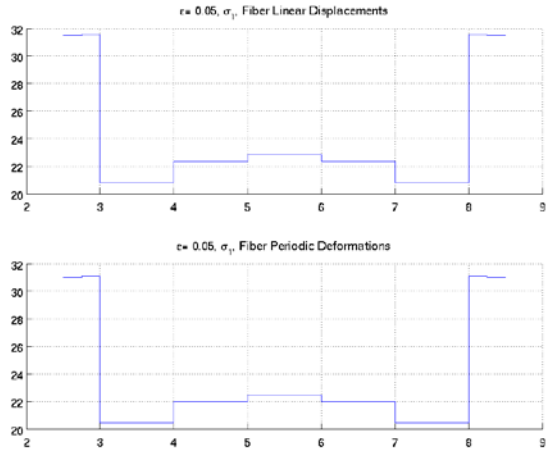

Figure 3-9
Axial Forces along the fiber in the deformed configuration

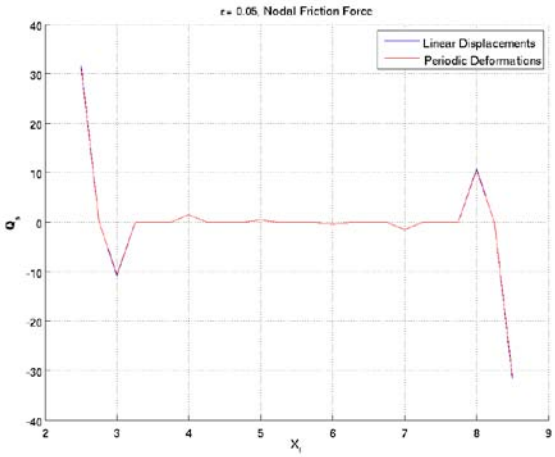

Figure 3-10
Nodal Friction force along the fiber in the undeformed configuration

Figures Figure 3-9and 3-10 represent the distribution of the axial forces of the fiber, as well as the nodal friction forces along the fiber.

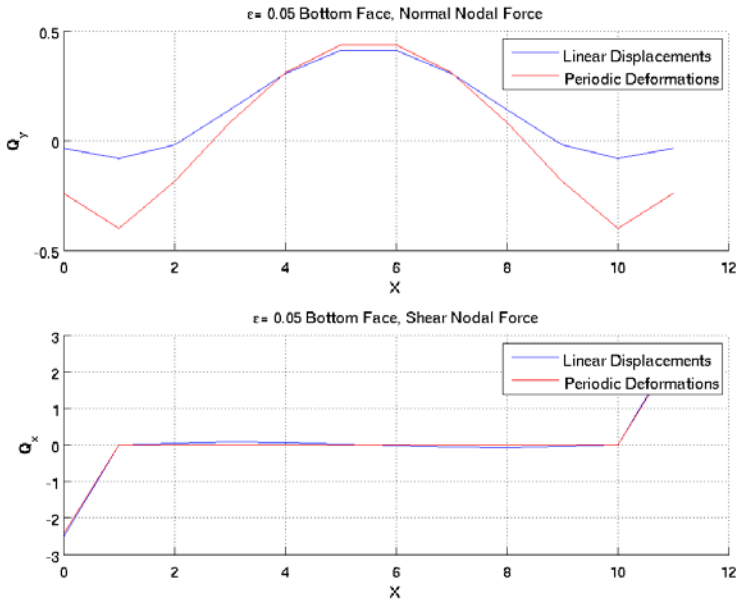

Figure 3-11
Boundary Nodal tractions along the Bottom Face of the RVE

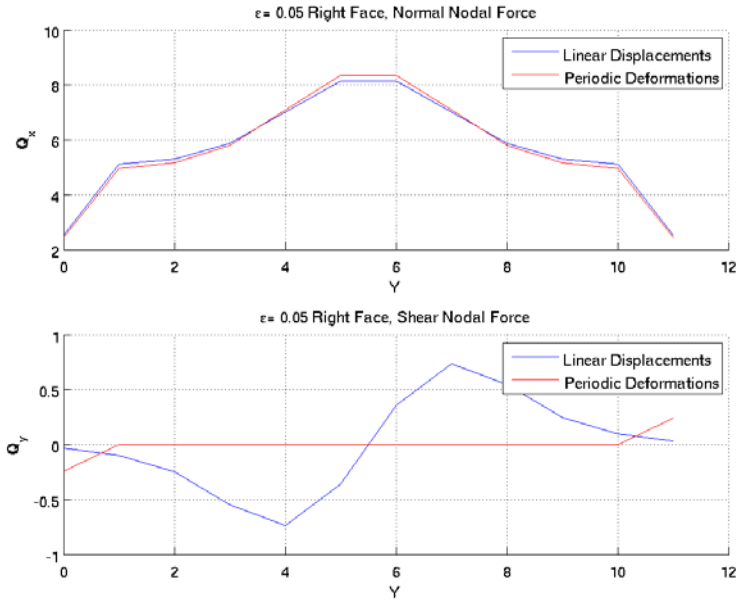

Figure 3-12
Boundary Nodal tractions along the Right Face of the RVE

The figures above depict the boundary nodal tractions for two of the faces of the RVE. There are noticeable differences between the two homogenization schemes, as far as the normal tractions at the bottom face and the shear tractions at the right face are concerned. The latter implies that the RVE, when analyzed using the Linear Prescribed Boundary Displacements, shows much

larger shear strain than when Periodic Boundary Displacements are prescribed; this leads to greater stiffness of the RVE in the first case.

3.1.2 Macroscopic Model

For the macroscopic configuration, we consider a cantilever beam of length 25.00 units, height 5.00 units and thickness $t = 1$, loaded with a vertical load of magnitude 1, scaled by a loading factor λ, which takes values from zero to 0.8. The configuration is represented in Figure 3-13.

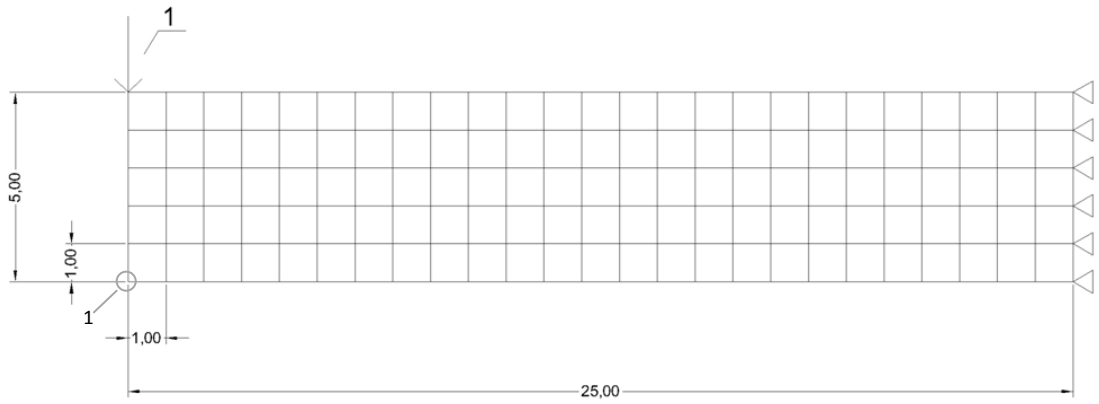

Figure 3-13

The results of the loading are presented subsequently.

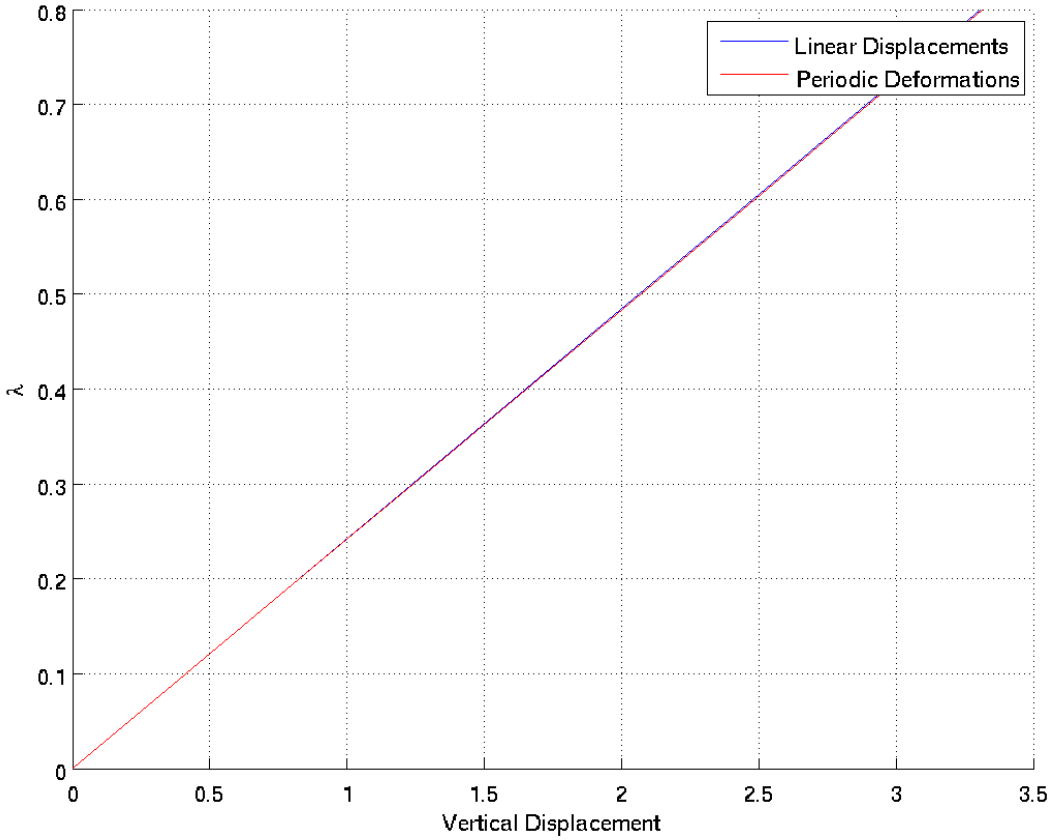

Figure 3-14
Variation of the loading factor λ with the vertical displacement of point 1

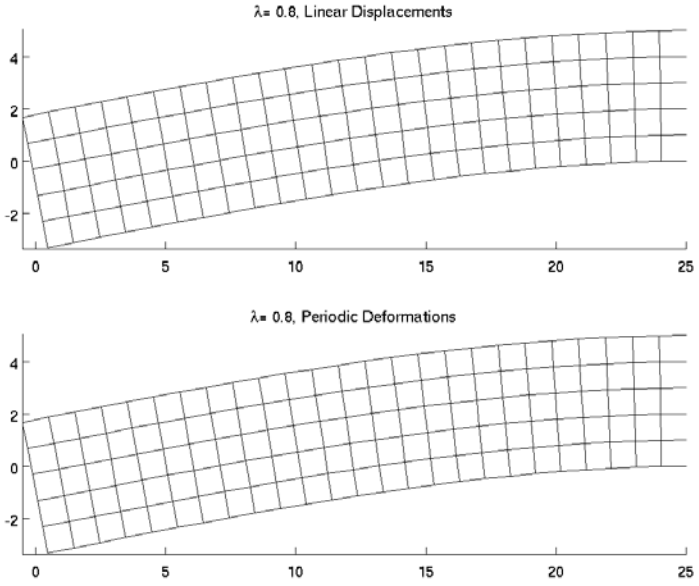

Figure 3-15
Deformed Shape for the two homogenization schemes

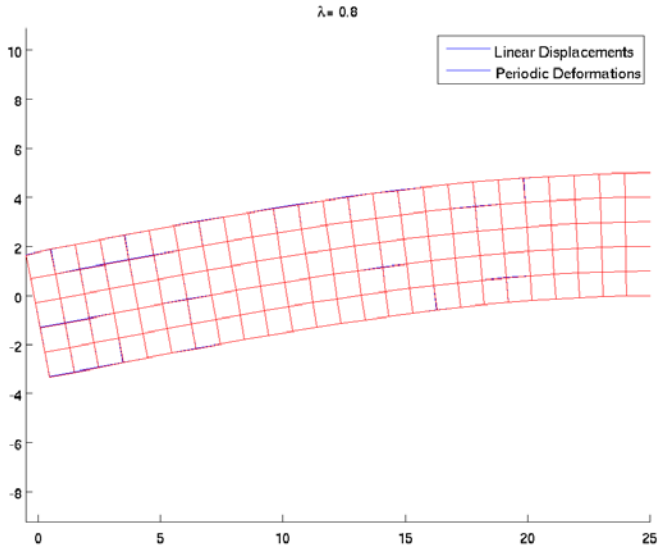

Figure 3-16

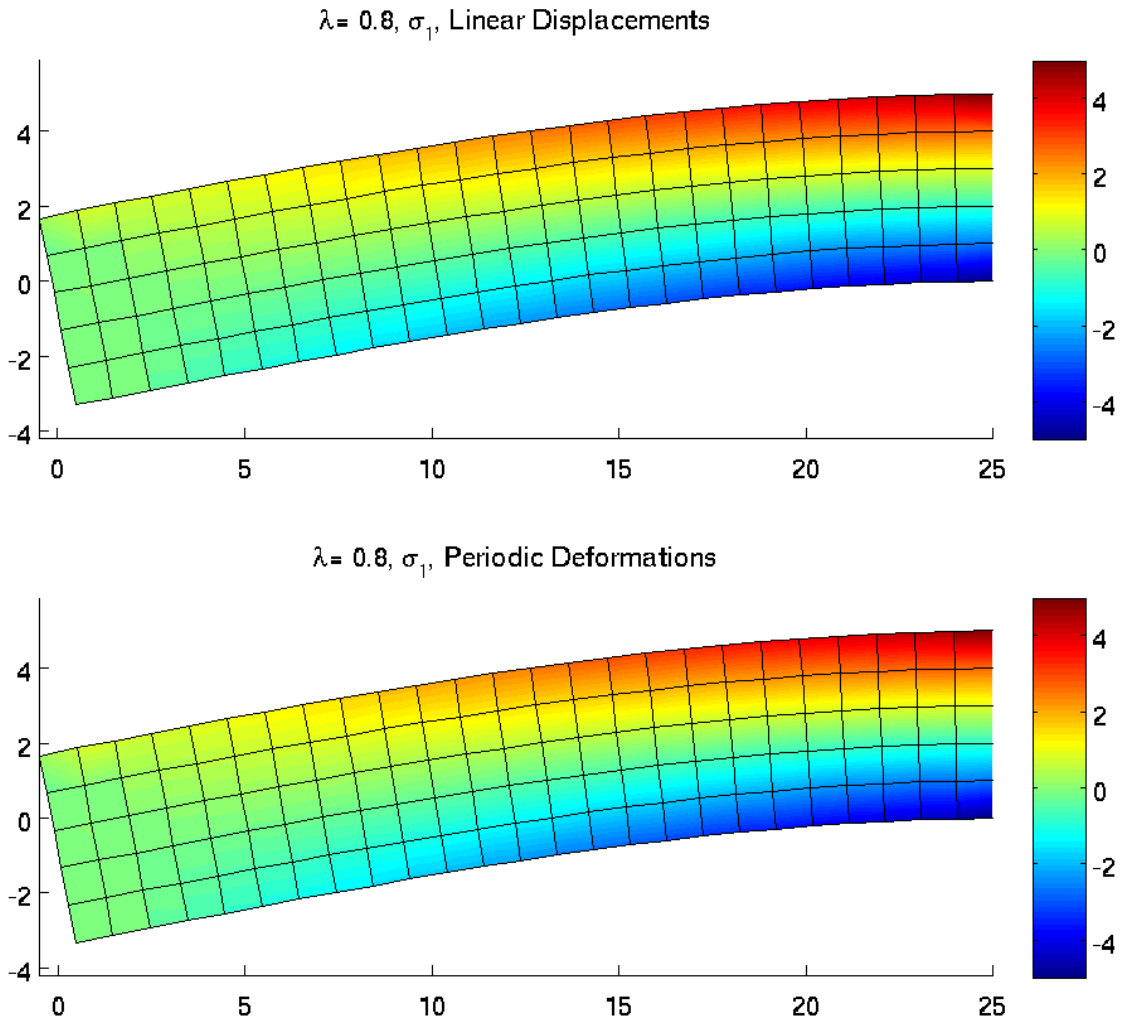

Figure 3-17
σ_{11} for the two Homogenization Schemes

Figures 3-14 and 3-17 show negligible differences of the stress state of the cantilever between the two homogenization schemes

3.2 Non-Elastic Modelling

3.2.1 Microscopic Model

3.2.1.1 Monotonic Loading

We consider the same configuration as the elastic model, only this time, slippage between the fiber and the matrix is allowed. The following bond stress-slip relation is considered:

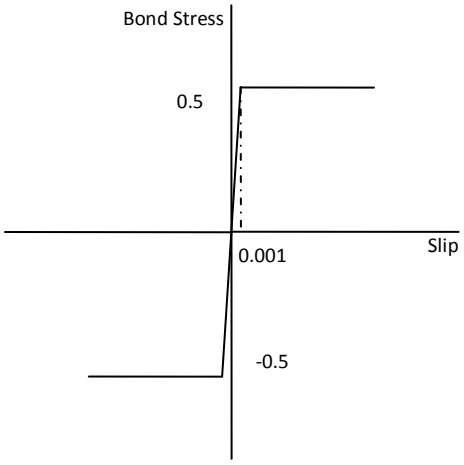

Figure 3-18

Kinematic hardening is assumed. The elastic branch stiffness is equal to 500units, and the plastic branch stiffness is equal to $5e-6$.

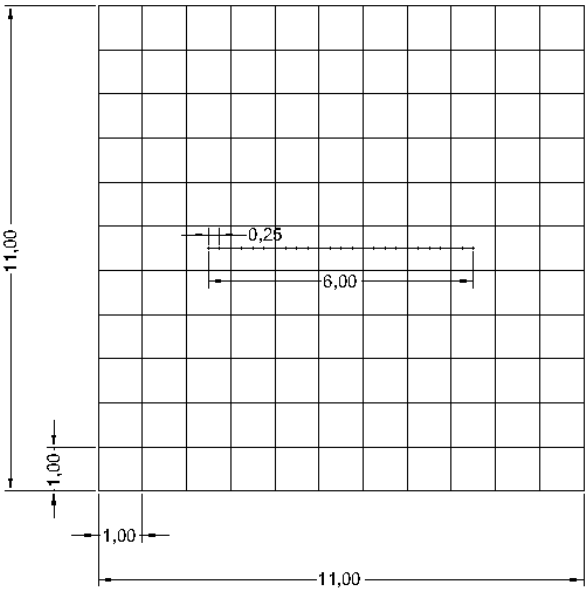

Figure 3-19
RVE configuration

Again, strain equal to $\{\varepsilon_{11} \quad \varepsilon_{22} \quad \gamma_{12}\}^T = \{\varepsilon_1 \quad -0.2\varepsilon_1 \quad 0\}^T$ is applied in increments of $\Delta\varepsilon_1 = 3.14e-4$ until the value $\varepsilon_1 = 0.05$ is reached.

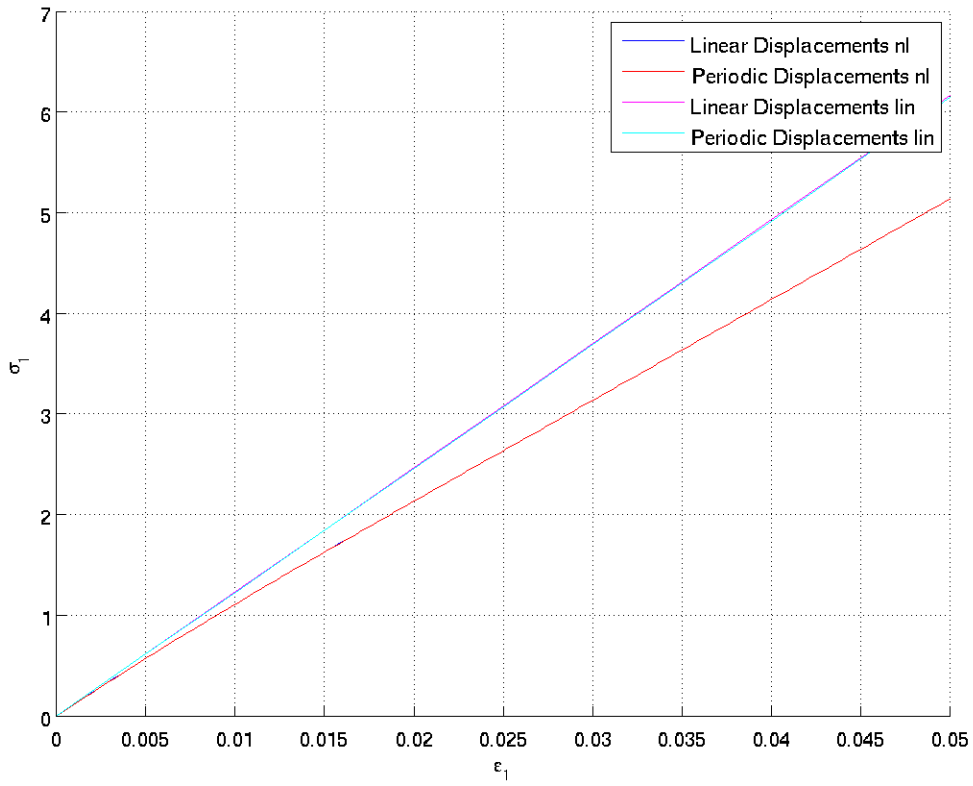

Figure 3-20
Stress-strain curve for x-direction($\sigma_1 - \varepsilon_1$)

The tangential elasticity matrices and stresses at $\varepsilon_1 = 0.05$ are equal to:

$$\mathbb{C}_{linear} = \begin{bmatrix} 104.16667 & 20.833333 & 4.773959E-15 \\ 20.833333 & 104.16667 & 2.1177504E-14 \\ -3.0481173E-13 & 6.6613381E-16 & 41.666667 \end{bmatrix}$$

$$\mathbb{C}_{periodic} = \begin{bmatrix} 104.16667 & 20.833333 & 6.6613381E-16 \\ 20.833333 & 104.16667 & 2.0251315E-14 \\ 2.1035385E-14 & 1.8638449E-14 & 41.666667 \end{bmatrix}$$

$$\sigma_{linear} = \begin{Bmatrix} 5.1318354 \\ -2.9682203E-15 \\ -5.5823401E-15 \end{Bmatrix}$$

$$\sigma_{periodic} = \begin{Bmatrix} 5.1318354 \\ 2.3895816E-15 \\ 2.0897832E-15 \end{Bmatrix}$$

Because the fiber has slipped in its entirety at strain $\varepsilon_1 = 0.05$, the tangential elasticity matrix of the RVE at that strain is practically identical to that of the material of the matrix.

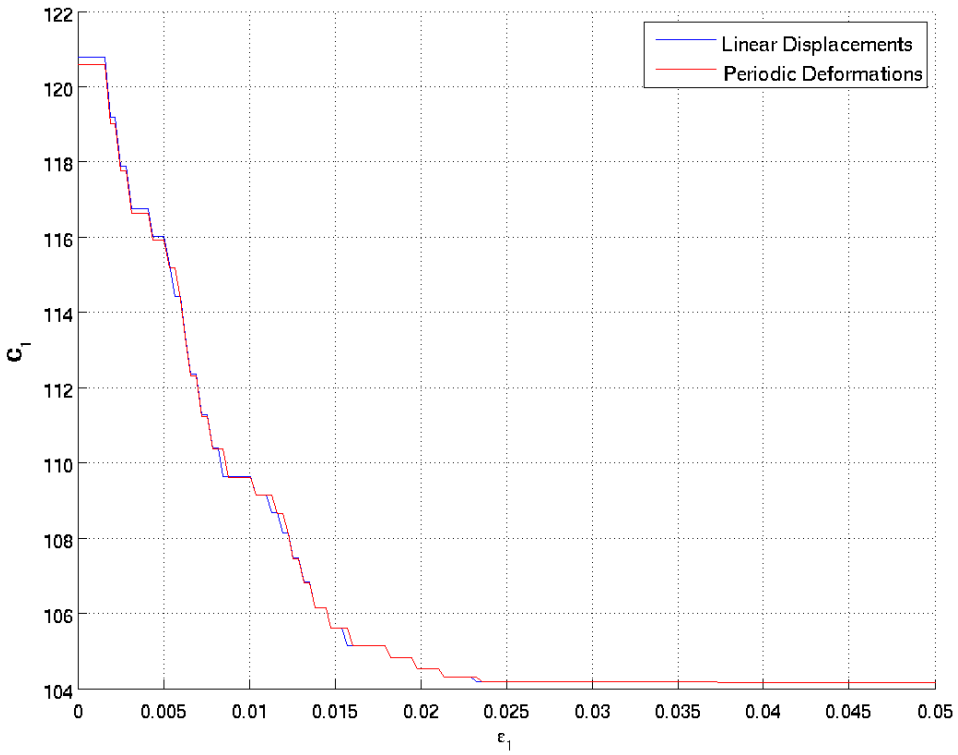

Figure 3-21
Variation of $\mathbb{C}_{11}$ Elastic Coefficient with strain ε_1

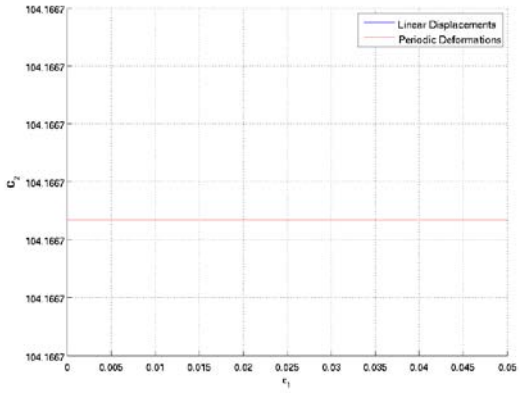

Figure 3-22
Variation of $\mathbb{C}_{22}$ Elastic Coefficient with strain ε_1

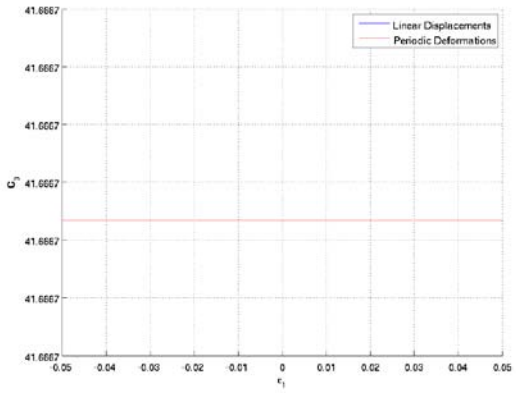

Figure 3-23
Variation of $\mathbb{C}_{33}$ Elastic Coefficient with strain ε_1

As can be observed from Figure 3-21, the $\mathbb{C}_{11}$ Elastic Coefficient decreases with strain until it reaches the value of the $\mathbb{C}_{11}$ of the material of the matrix. The steps that the elasticity presents as it decreases are due to the discretization error; each step corresponds to the complete slip of a fiber element.

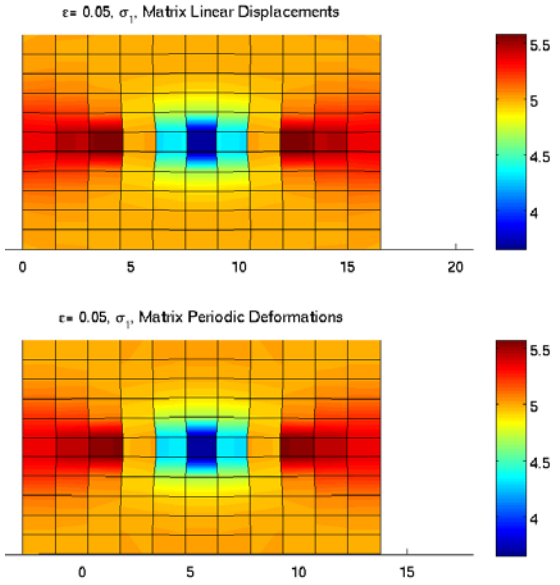

Figure 3-24
Stress σ_{11} for $\varepsilon_1 = 0.05$, Linear and Periodic Prescribed Boundary Deformations

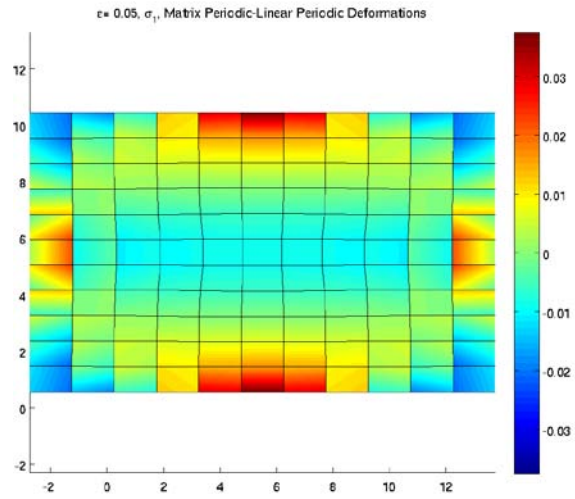

Figure 3-25
Stress σ_{11} for $\varepsilon_1 = 0.05$, Difference between Periodic and Linear Prescribed Boundary Deformations

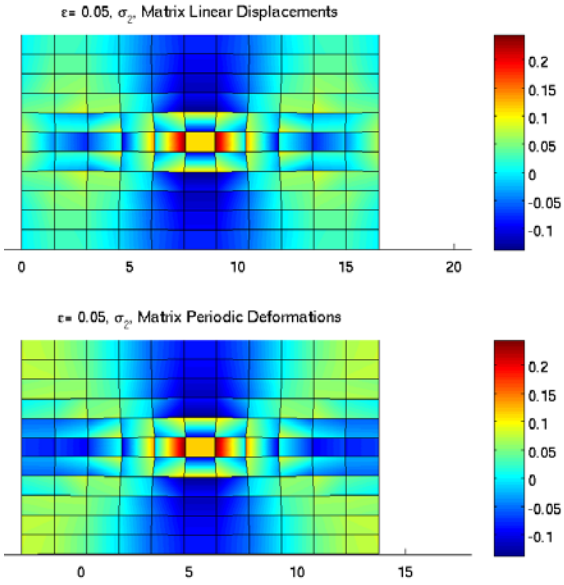

Figure 3-26
Stress σ_{22} for $\varepsilon_1 = 0.05$, Linear and Periodic Prescribed Boundary Deformations

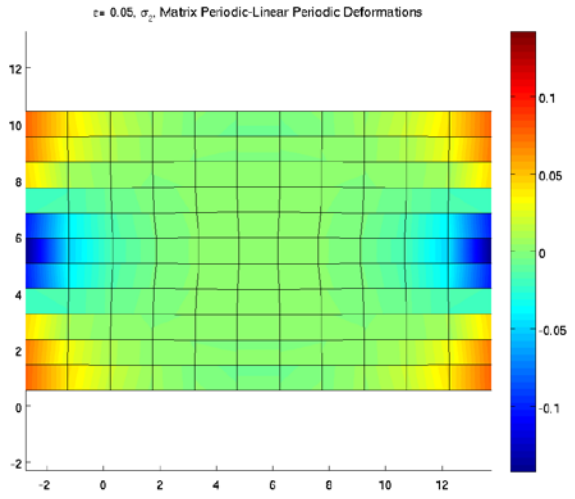

Figure 3-27
Stress σ_{22} for $\varepsilon_1 = 0.05$, Difference between Periodic and Linear Prescribed Boundary Deformations

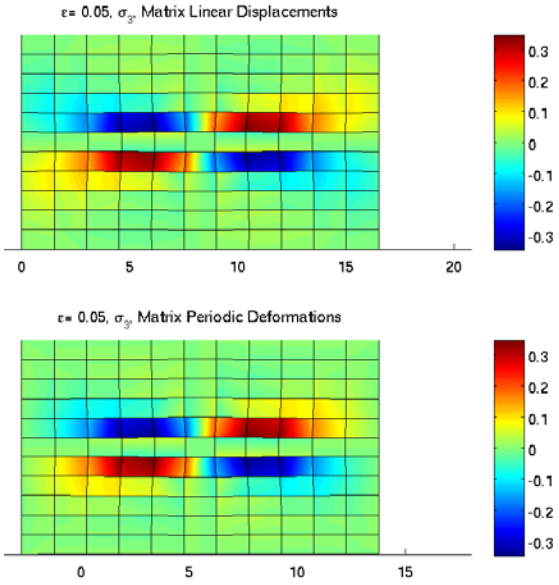

Figure 3-28
Stress τ_{12} for $\varepsilon_1 = 0.05$, Linear and Periodic Prescribed Boundary Deformations

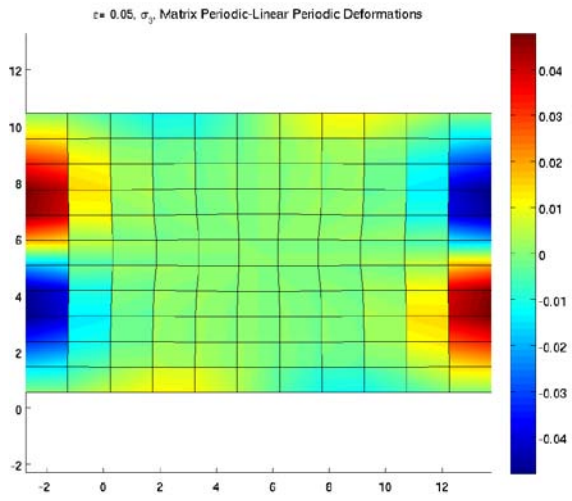

Figure 3-29
Stress τ_{12} for $\varepsilon_1 = 0.05$, Difference between Periodic and Linear Prescribed Boundary Deformations

Observing figures 3-26 and 3-29, the decrease of the σ_{22} as well as of the τ_{12} stresses in relation to their counterparts in the elastic configuration is noticeable (see fig. 3-3 and 3-8) . As far as the σ_{11}stresses are concerned, these have become much more uniform in comparison to the elastic state; their average value hasn't changed significantly, though.

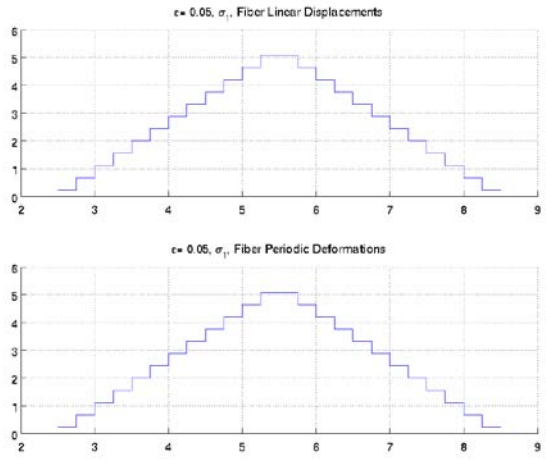

Figure 3-30
Axial Forces along the fiber in the deformed configuration

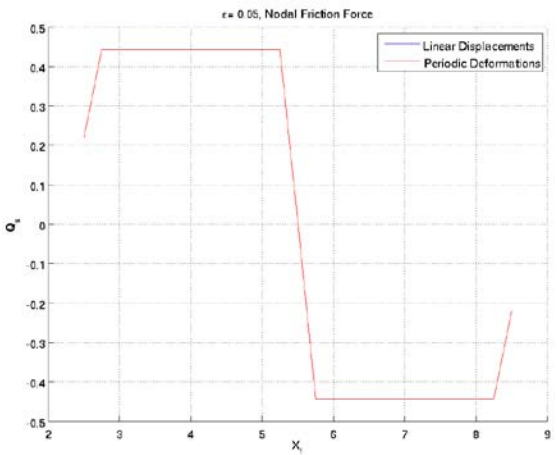

Figure 3-31
Nodal Friction force along the fiber in the undeformed configuration

As far as friction is concerned, due to the complete slippage of the fiber, friction has reached its maximum value, equal to 0.5 from edge to edge of the fiber.

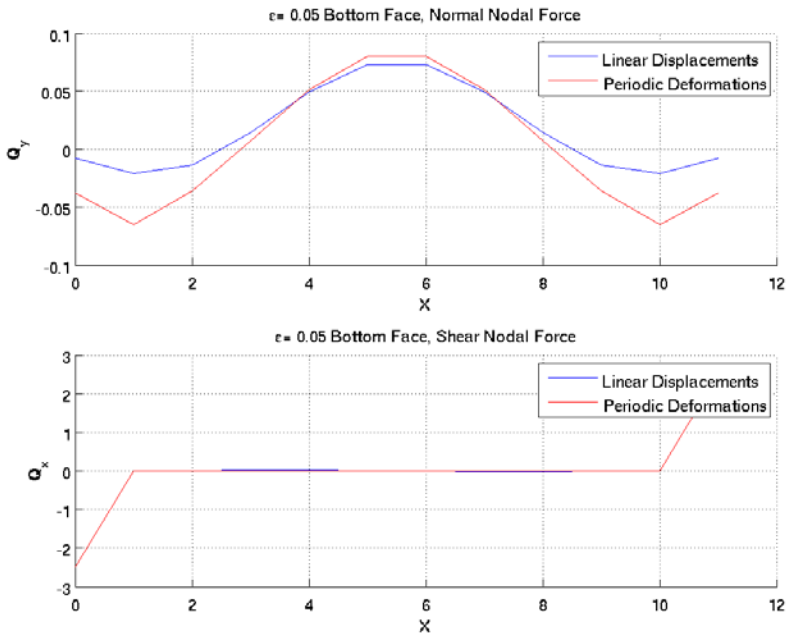

Figure 3-32
Boundary Nodal tractions along the Bottom Face of the RVE

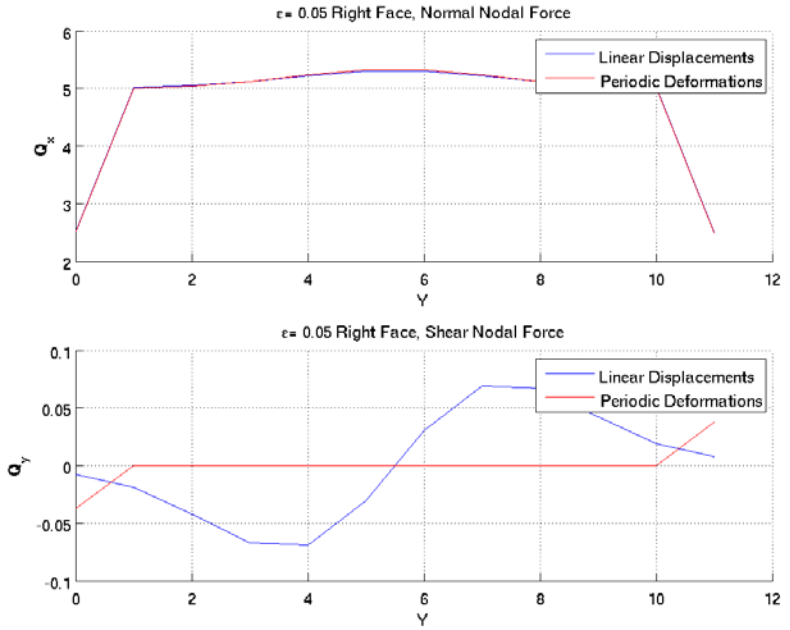

Figure 3-33
Boundary Nodal tractions along the Right Face of the RVE

It can be gathered from fig. 3-32 and 3-33 that the “parasitic” tractions (that is, the normal tractions acting upon the bottom face and the shear tractions acting upon the right face), although still existent, have decreased significantly in comparison to the elastic state (see fig. 3-11 and 3-12. Moreover, the normal traction acting upon the right face has become more uniform, resembling that of a homogeneous material.

3.2.1.2 Cyclic Loading

This time, the strain is not applied monotonically, but in steps of $\Delta\varepsilon_1 = 3.14e-4$ until a full cycle between the values $\varepsilon_1 = 0.05$ and $\varepsilon_1 = -0.05$ is achieved. The results are displayed below.

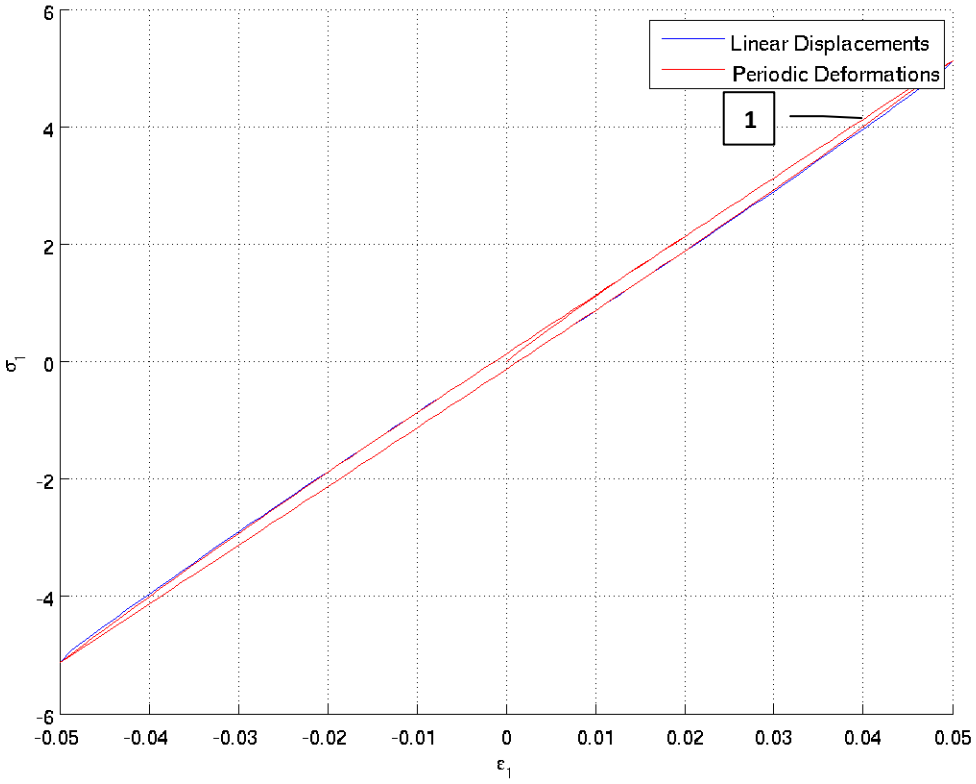

Figure 3-34
Stress-strain curve for x-direction($\sigma_1 - \varepsilon_1$)

Two states are contrasted, State 1 and State 2 (see Figure 3-34).

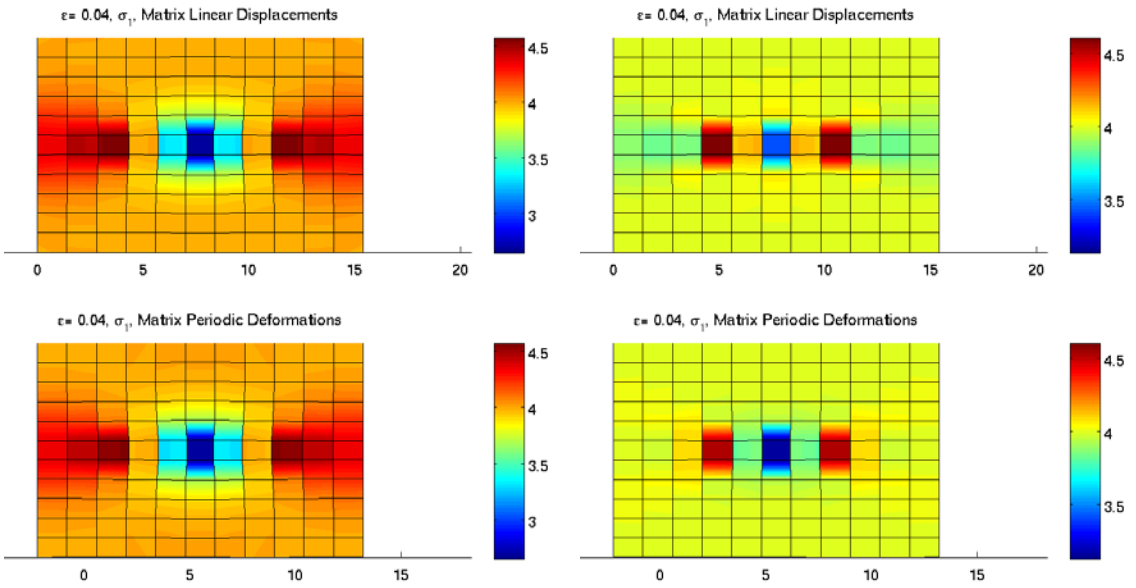

Figure 3-35
Stress σ_{11} for $\varepsilon_1 = 0.05$, Linear and Periodic Prescribed Boundary Deformations, State 1

Figure 3-36
Stress σ_{11} for $\varepsilon_1 = 0.05$, Linear and Periodic Prescribed Boundary Deformations, State 2

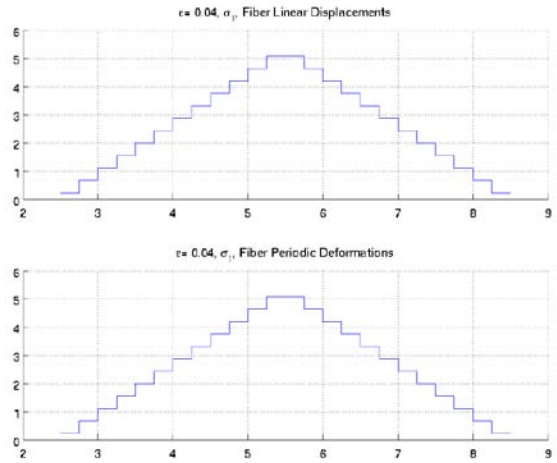

Figure 3-37
Axial Forces along the fiber in the deformed configuration, State 1

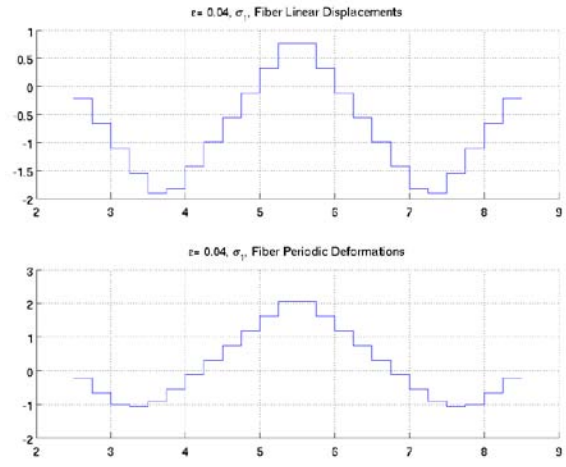

Figure 3-38
Axial Forces along the fiber in the deformed configuration, State 2

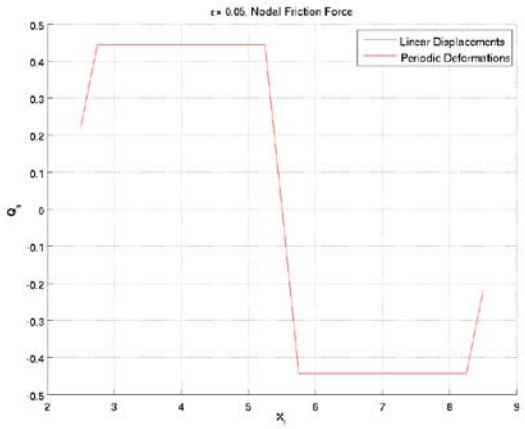

Figure 3-39
Nodal Friction force along the fiber in the undeformed configuration, State 1

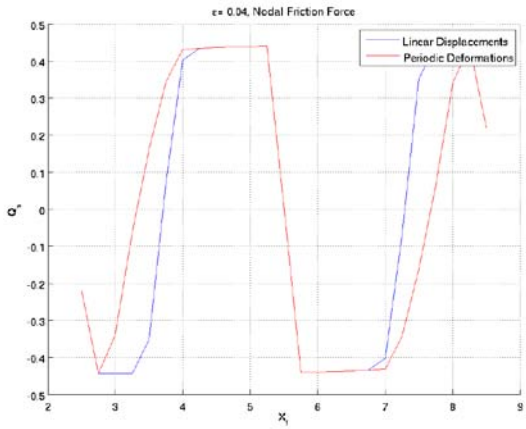

Figure 3-40
Nodal Friction force along the fiber in the undeformed configuration, State 2

The difference in the nodal friction between the two homogenization schemes is due to numerical instabilities, which diminish as the loading continues.

3.2.2 Macroscopic Loading

The macroscopic structure used in the elastic modelling is considered to consist of a microstructure represented by the RVE described in the previous section. The same load as before is applied, and the results are presented below.

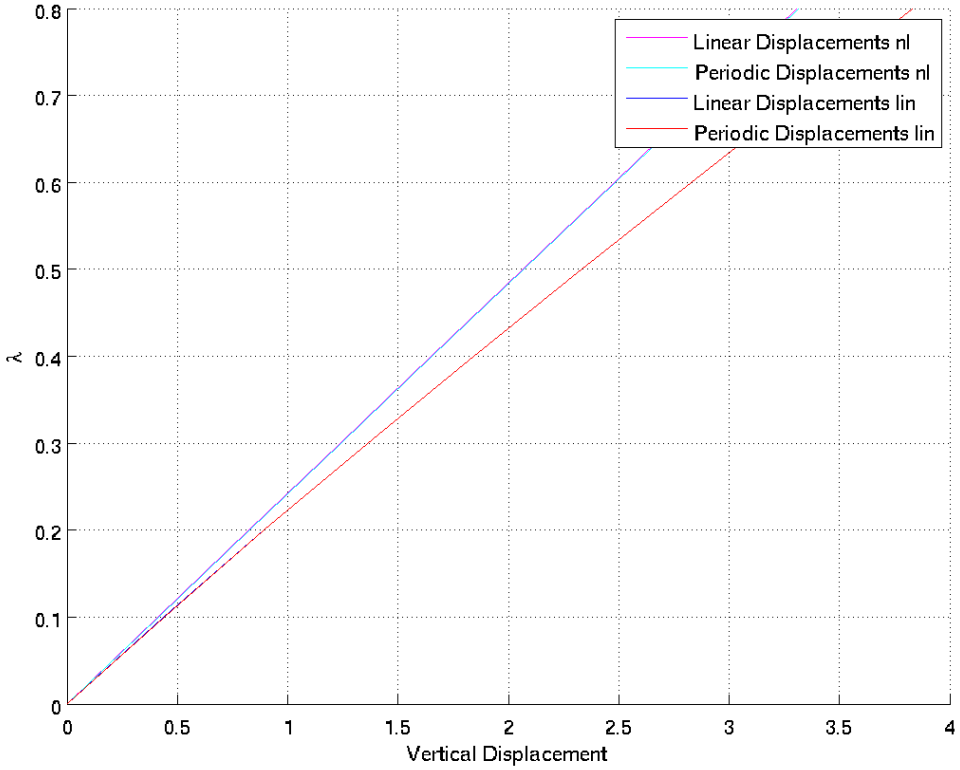

Figure 3-41
Variation of the loading factor λ with the vertical displacement of point 1

3.2.2.1 *Last Step*

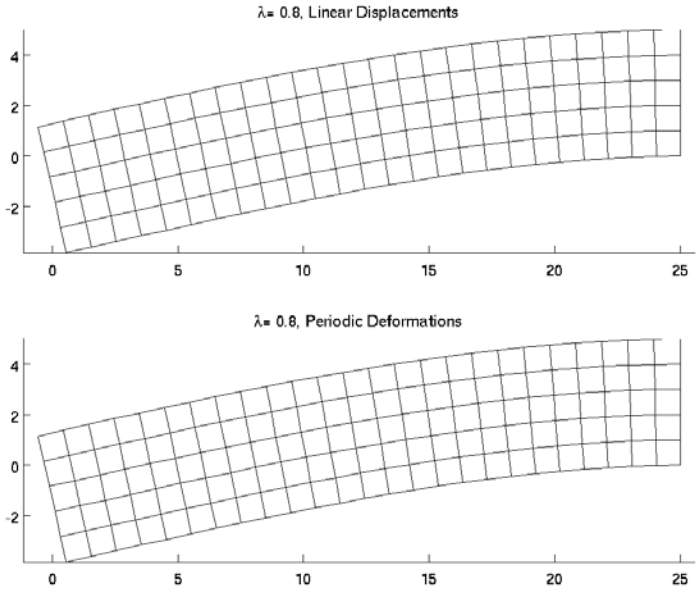

Figure 3-42
Deformed Shape for the two homogenization schemes

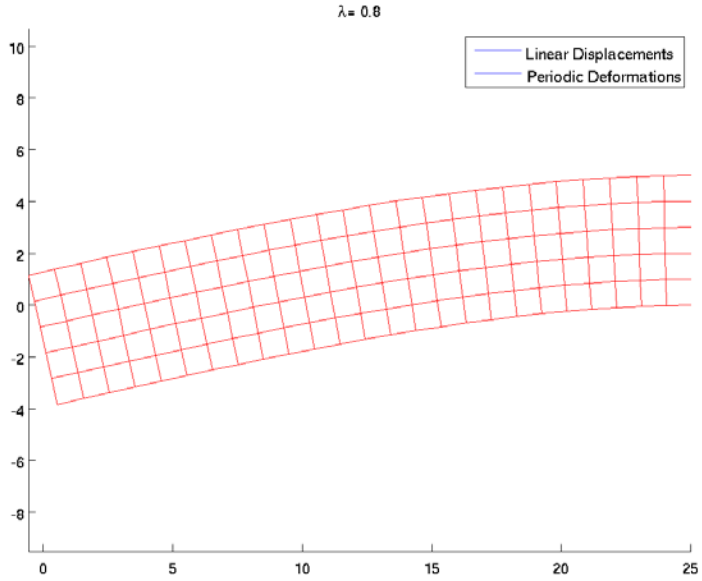

Figure 3-43
Superposition of the Deformed Shape for the two homogenization schemes
(blue denotes the Liner Displacement Scheme, red the Periodic Deformation Scheme)

Above is presented the deformed shape of the structure for the two homogenization schemes. The two configurations practically coincide.

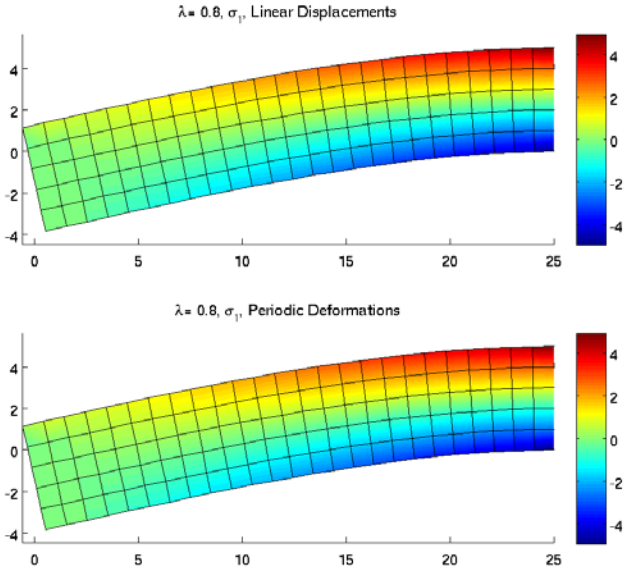

Figure 3-44
Stress σ_{11} for $\lambda = 0.8$, Linear and Periodic Prescribed Boundary Deformations

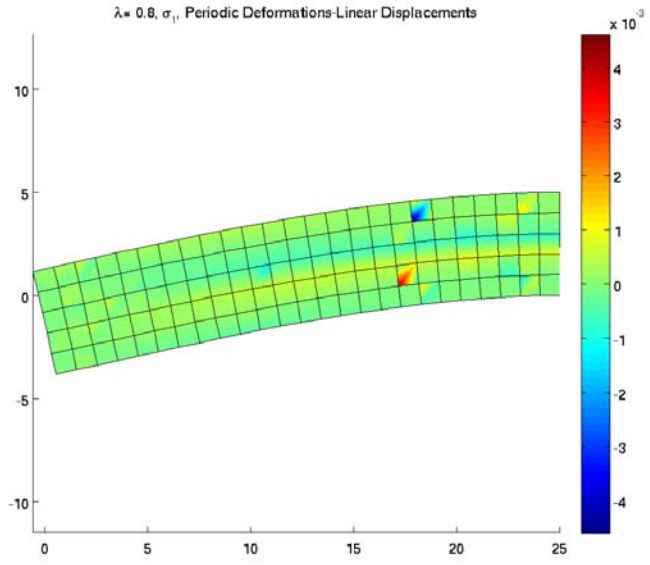

Figure 3-45
Stress σ_{11} for $\lambda = 0.8$, Difference between Periodic and Linear Prescribed Boundary Deformations

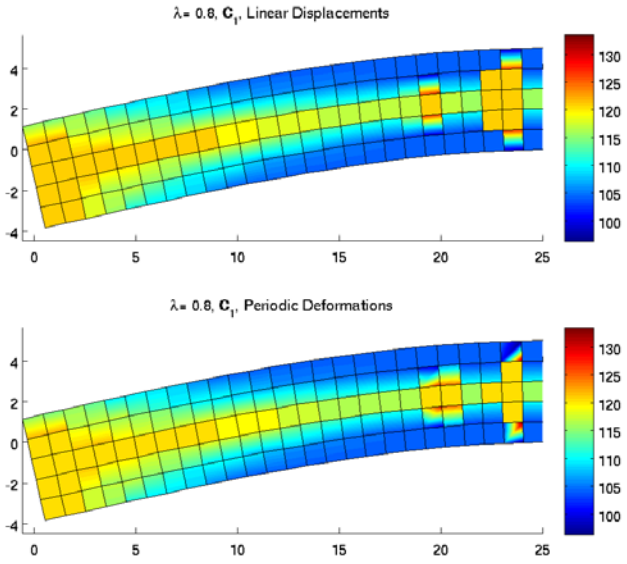

Figure 3-46
Elastic coefficient $\mathbb{C}_{11}$ for $\lambda = 0.8$, Linear and Periodic Prescribed Boundary Deformations

From Fig. 3-44 and 3-45 it can be deduced that the σ_{11}stress field practically coincides for the two configurations.

As far as Figure 3-46 is concerned, value of $\mathbb{C}_{11}$ equal to 104.16 denotes that the fiber has slipped completely. From the above it is obvious that for a large portion of the structure slippage has occurred. (It should be noted here that the random localized stiffening of some areas in the “plastic” region can be attributed to numerical instabilities).

3.2.2.2 Previous Steps

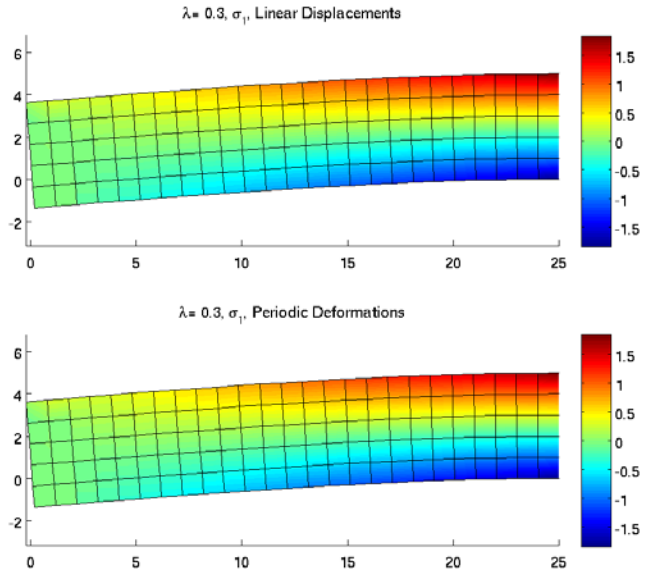

Figure 3-47
Stress σ_{11} for $\lambda = 0.3$, Linear and Periodic Prescribed Boundary Deformations

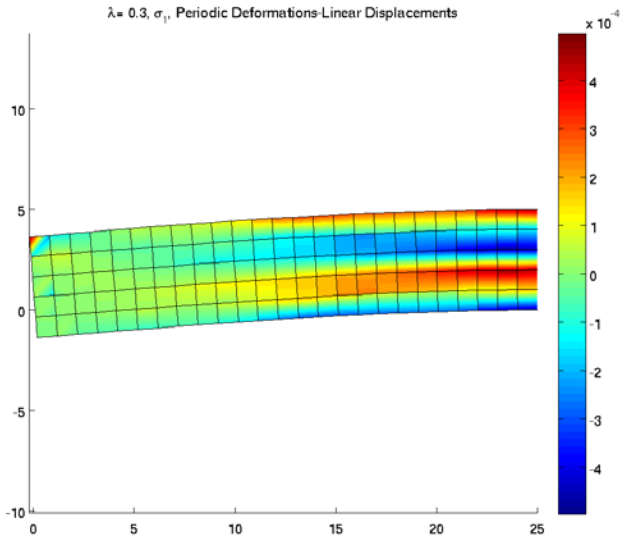

Figure 3-48
Stress σ_{11} for $\lambda = 0.3$, Difference between Periodic and Linear Prescribed Boundary Deformations

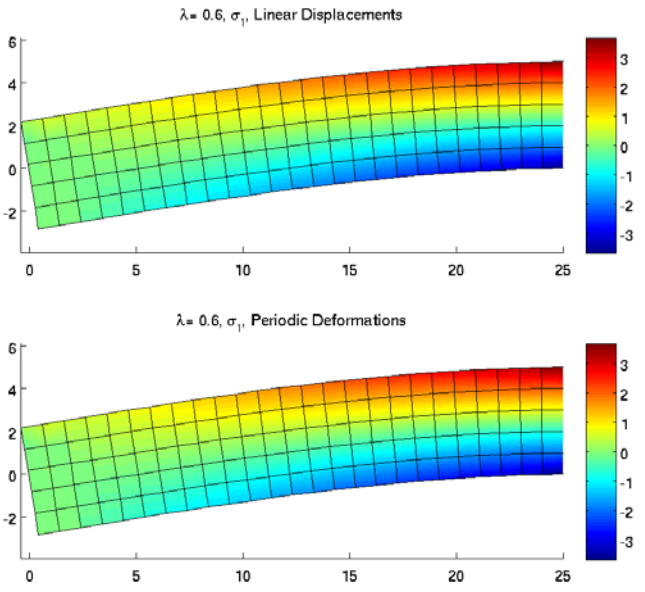

Figure 3-49
Stress σ_{11} for $\lambda = 0.6$, Linear and Periodic Prescribed Boundary Deformations

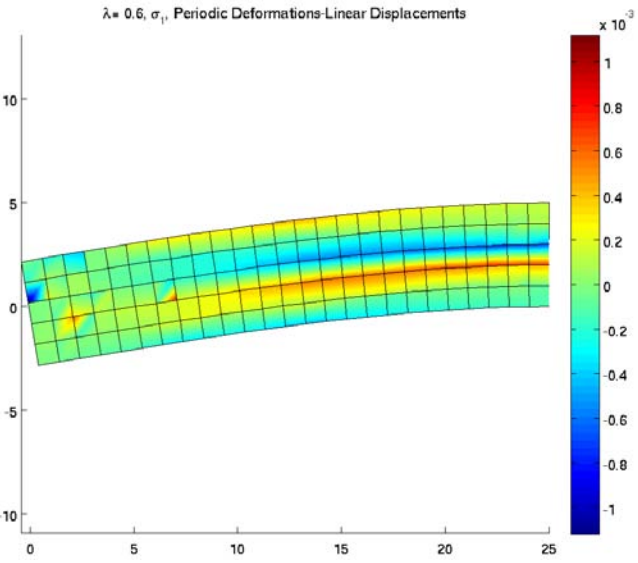

Figure 3-50
Stress σ_{11} for $\lambda = 0.6$, Difference between Periodic and Linear Prescribed Boundary Deformations

From the figures above it becomes obvious that, as the fibers of the microscopic structure at a point in the macroscopic configuration begin to slip, differences arise in the stresses calculated with the two homogenization schemes. That is, when periodic displacements are prescribed to the RVE boundary, the σ_{11} stress tends to be somewhat larger at the flange and smaller towards the middle of the beam cross-section, in relation to its counterpart when linear displacements

are prescribed. However, this difference declines with the increase of the imposed macroscopic load.

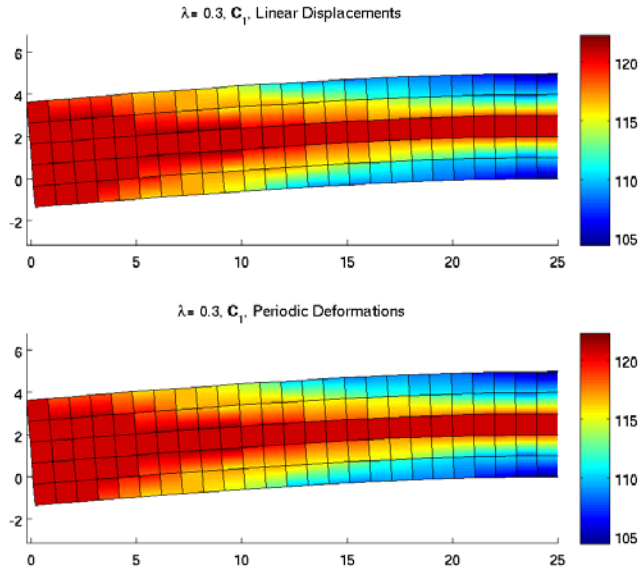

Figure 3-51
Stress σ_{11} for $\varepsilon_1 = 0.05$, Linear and Periodic Prescribed Boundary Deformations

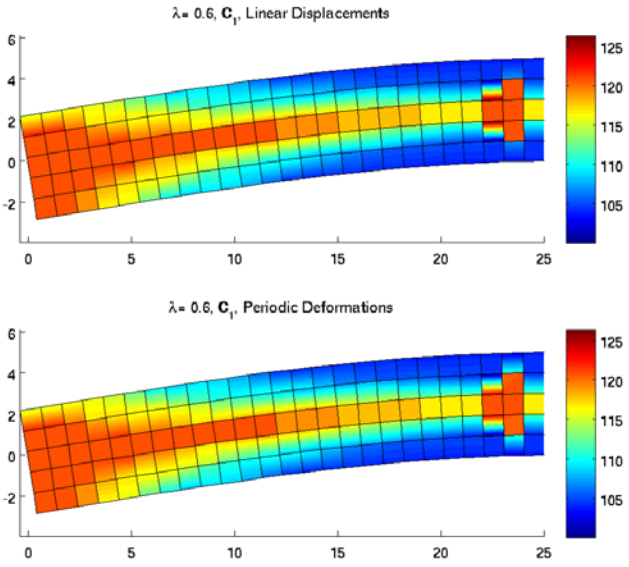

Figure 3-52
Stress σ_{11} for $\varepsilon_1 = 0.05$, Difference between Periodic and Linear Prescribed Boundary Deformations

4 Conclusions

We have examined, in the scope of this thesis, the application of the first-order homogenization scheme, as proposed by (Miehe & Koch, 2002), within a macroscopic framework; in particular, how these methods are integrated with a bond-slip mathematical description.

In the course of this treatise, it was shown that there are minimal differences between the linear and the periodic prescribed boundary displacements, at the microscopic as well as the macroscopic level. Whatever small differences exist can be ascribed to the fact that the homogenization pertaining to periodic boundary displacements can approximate more closely uniform stress conditions, in contrast to the linear boundary displacements method, by which additional, parasitic stresses are introduced (in our case, shear), thus causing an artificial "stiffening" of the material.

Aside from that, it was concluded that in our particular case, the model used displays non-linearity mainly in one direction (the direction of the fiber). Whatever collateral non-linearity exists in the transverse direction was effectively dampened by the homogenization scheme; thus, in this case, the use of a sequential analysis method in conjunction with a homogenization scheme could produce comparable results to the more computationally intensive nested solution scheme.

Lastly, on a note about the stability of the results, it should be mentioned that the use of the model of friction described in this thesis with the bond-slip model is susceptible to numerical instabilities. Special attention should be paid to the mathematical description of friction, especially when the bond slip model is used within the framework of a homogenization scheme.

Appendix –Line Search Method

Let us consider the set of nonlinear equations

$$\boldsymbol{F}(\boldsymbol{t}) = \boldsymbol{0}, \tag{0.1}$$

and let $\boldsymbol{t_k}$ be the value of the variables at the end of step k of the Newton-Raphson method, and $\boldsymbol{l}$ the change of the value of $\boldsymbol{t}$ at the k+1 step of the Newton-Raphson, such that

$$\boldsymbol{t_{k+1}} = \boldsymbol{t_k} + \boldsymbol{l}, \tag{0.2}$$

where

$$\nabla_{\boldsymbol{t}} \boldsymbol{F}(\boldsymbol{t_k}) \cdot \boldsymbol{l} = -\boldsymbol{F}(\boldsymbol{t_k}) \tag{0.3}$$

We consider a scalar "potential energy" function $\Pi(\mathbf{t})$, such that

$$\nabla_{\mathbf{t}} \Pi = \boldsymbol{F} \tag{0.4}$$

The line-search methodology states that instead of applying the step $\boldsymbol{l}$ to the value $\boldsymbol{t_k}$, we apply a fraction of it $a \cdot \boldsymbol{l}$, such that the function P is minimized at point $\boldsymbol{t} = \boldsymbol{t_k} + a \cdot \boldsymbol{l}$.

The above condition is equivalent to:

$$\frac{\partial \Pi}{\partial a} = 0 \Leftrightarrow \nabla_{\mathbf{t}} \Pi \cdot \frac{d\boldsymbol{t}}{da} = 0 \Leftrightarrow \boldsymbol{F}(\boldsymbol{t_k} + a\boldsymbol{l}) \cdot \boldsymbol{l} = 0 \tag{0.5}$$

We introduce the function $r(a)$ as

$$r(a) = \boldsymbol{F}(\boldsymbol{t_k} + a\boldsymbol{l}) \cdot \boldsymbol{l} \tag{0.6}$$

Thus, 0.5 can be rewritten as:

$$r(a) = 0 \tag{0.7}$$

We usually don't seek an exact solution of the above equation, but a value a such that:

$$|r(a)| \leq \rho |r(0)| \tag{0.8}$$

Where $0.1 \leq \rho \leq 0.9$, and generally takes the value 0.5.

One common technique used for the solution of Eq. 0.7 is the approximation of r with a second-order polynomial $p(a)$, such that $p(0) = r(0)$, $\frac{dp}{da}(0) = \frac{dr}{da}(0)$ and $p(1) = r(1)$.

It is:

$$\frac{dr}{da}(0) = \nabla_{\boldsymbol{t}} \boldsymbol{F}(\boldsymbol{t_k} + \boldsymbol{0} \cdot \boldsymbol{l}) \cdot \boldsymbol{l} \overset{0.3}{=} -\boldsymbol{F}(\boldsymbol{t_k}) \cdot \boldsymbol{l} = -r(0) \quad 0.9$$

Thus, $p(a)$ is equal to:

$$p(a) = (1 - a) \cdot r(0) + r(1) \cdot a^2 \quad 0.10$$

The roots of the above equation are equal to:

$$a = \frac{\eta}{2} \pm \sqrt{\left(\frac{\eta}{2}\right)^2 - \eta}\,, \quad \eta = \frac{r(0)}{r(1)} \quad 0.11$$

If $\eta < 0 \; or \; \eta > 4$, the root of the above equation is real and equal to:

$$a_1 = \frac{\eta}{2} + \sqrt{\left(\frac{\eta}{2}\right)^2 - \eta} \quad 0.12$$

If $0 < \eta < 4$, then there isn't a real root of p, and we choose the value of a that minimizes p, that is:

$$a_1 = \frac{\eta}{2} \quad 0.13$$

After we select a value of a_1, we check condition 0.8. If the condition is satisfied, then we calculate $\boldsymbol{t_{k+1}} = \boldsymbol{t_k} + a_1 \cdot \boldsymbol{l}$, and we move to the next iteration of the Newton-Raphson method.

If not, then we repeat the procedure, approximating $r(a)$ with a polynomial such that $p(0) = r(0), \frac{dp}{da}(0) = \frac{dr}{da}(0)$ and $p(a_1) = r(a_1)$.

The polynomial p can be calculated as:

$$p(a) = (a_1 - a) r(0) + r(a_1) \cdot \left(\frac{a}{a_1}\right)^2 \quad 0.14$$

And its roots are equal to:

$$a_2 = a_1^2 \left(\frac{\eta}{2} + \sqrt{\left(\frac{\eta}{2}\right)^2 - \frac{\eta}{a_1}} \right), \qquad \eta = \frac{r(0)}{r(a_1)} \quad 0.15$$

If $\left[\left(\frac{\eta}{2}\right)^2 - \frac{\eta}{a_1}\right] < 0$, then we select the value of a that minimizes p, that is:

$$a_2 = \frac{a_1^2 \eta}{2} \quad 0.16$$

Then we check condition 0.8. If the condition is satisfied, then we calculate $\boldsymbol{t_{k+1}} = \boldsymbol{t_k} + a_2 \cdot \boldsymbol{l}$ and we move to the next iteration of the Newton-Raphson method.

If not, then we repeat the procedure, substituting $a_1$with a_2, until the condition 0.8 is satisfied.

Bibliography

Feyel, F. (2003). A multilevel finite element method (FE2) to describe the response of highly non-linear structures using generalized continua. *ELSEVIER* , 12.

Kouznetsova, V. G. (2002). *Computational homogenization for the multi-scale analysis of multi-phase materials.*

Lykidis, G. C., & Spiliopoulos, K. V. (2008). 3D Solid Finite-Element Analysis of Cyclically Loaded RC Structures Allowing Embedded Reinforcement Slippage. *JOURNAL OF STRUCTURAL ENGINEERING* , 629-638.

Miehe, C., & Koch, A. (2002). Computational micro-to-macro transitions of discretized microstructures undergoing small strains. *Springer-Verlag* , 300-317.

Papadrakakis, M. (2001). *Αναλυση Φορέων με τη Μέθοδο των Πεπερασμένων Στοιχείων.* Αθήνα: Παπασωτηρίου.

Papadrakakis, M. (1996). *ΜΑΘΗΜΑΤΑ ΣΤΑΤΙΚΗΣ V.* Αθήνα: ΕΜΠ.

Papadrakakis, M. (1998). *Μη γραμμικά Πεπερασμένα Στοιχεία.* Αθήνα.

Wriggers, P., & Moftah, S. (2005). Mesoscale models for concrete: Homogenisation and damage behaviour. *Finite Elements in Analysis and Design* , 623-636.

Μωυσίδης, Α. (2012). *Μέθοδοι Πολλαπλών Κλιμάκων στην Επίλυση Ελαστοπλαστικών Προβλημάτων Επίπεδης Έντασης.* Αθήνα.